Optimized Modulation and Dynamic Control of a Three-Phase Dual Active Bridge Converter With Variable Duty Cycles

Jun Huang, Zhuoqiang Li, Ling Shi, Yue Wang, *Member, IEEE*, and Jinda Zhu

***Abstract*—The three-phase dual active bridge (3p-DAB) converter is a promising topology for high power dc–dc conversion due to advantages of bidirectional power flow, inherent soft-switching capability, and reduced filter volume. This paper presents comprehensive analysis of the duty cycle control (DCC) for optimizing the performance of the 3p-DAB. Based on DCC, an optimized modulation strategy is proposed to minimize the conduction losses of the 3p-DAB in the whole load range. The proposed modulation strategy extends the soft-switching range of the 3p-DAB with large voltage variations simultaneously. It is established through loss analysis that the proposed modulation strategy boosts the efficiency of the 3p-DAB, especially at low loads. When the duty cycles change fast as a result of the abruptly changed transmission power, the transformer currents can become unbalanced, leading to the magnetic bias and oscillations in dc currents. This paper further proposes a fast transient current control (FTCC) method for the 3p-DAB with variable duty cycles. The FTCC enables the converter to transfer from one steady state to another within about one-third switching period, hence balancing the transformer currents rapidly and avoiding oscillations in dc currents. Finally, experimental results verify the outstanding performance of the proposed modulation strategy and FTCC method.**

***Index Terms*—Duty cycle control (DCC), fast transient current control (FTCC), optimized modulation strategy, soft switching, three-phase dual active bridge (3p-DAB).**

NOMENCLATURE

V_1, V_2	DC port voltage.
I_1, I_2	Port current.
C_1, C_2	DC capacitor.
T_{xy} $(x = 1, 2, y = 1, 2 \ldots 6)$	Active switch, e.g., power MOSFET.
D_{pxy} $(x = 1, 2, y = 1, 2 \ldots 6)$	Antiparallel diode.
N_{12}	Turns ratio of the transformer.

Manuscript received December 2, 2017; revised April 4, 2018; accepted May 18, 2018. Date of publication May 29, 2018; date of current version February 5, 2019. This work was supported by Nari Group Corporation R&D Program under Grant 52460817A036. Recommended for publication by Associate Editor L. Corradini. *(Corresponding author: Jun Huang.)*

J. Huang and J. Zhu are with Nari Group Corporation (State Grid Electric Power Research Institute), Nanjing 211000, China (e-mail:

transformers, medium-voltage dc transmission systems, electric vehicles, and auxiliary power supplies for railways [1]–[5]. The three-phase dual active bridge (3p-DAB), a promising topology of the IBDC, is originally proposed for high-power dc–dc conversion in [6]. The 3p-DAB consists of two three-phase active bridges and a high-frequency three-phase transformer with Y/Y connection. The topology has advantages of electrical isolation, bidirectional power flow, and inherent soft-switching capability [7]–[9]. It also has lower device stress, lower transformer kVA rating, and reduced filter volume as a result of smaller ripple current in dc capacitors compared with the single-phase topology [10], [11].

The conventional modulation strategy for the 3p-DAB is the phase-shift (PS) control, which is widely used due to the simple operation and inherent zero-voltage switching (ZVS) capability without adding any extra passive components. However, the ZVS operating range is limited when the voltage conversion ratio is away from unity. The hard-switching (HS) operation occurs under light load conditions, and the efficiency of the converter decreases consequently [6], [12], [13]. In addition, the conduction losses are not optimized under PS control. Therefore, PS control is not effective in applications that require large voltage variations and wide load ranges. The same conclusions can be found in the single-phase DAB (1p-DAB). In order to overcome inherent drawbacks of PS control, numerous modulation strategies have been developed for the 1p-DAB. Introducing the inner PS angle is the most common method that derives the optimized modulation in 1p-DAB applications [14]–[18]. Nevertheless, it is difficult to realize the adjustable PS angle between two phase legs due to the 120° PS angle among three phases of the 3p-DAB. The approaches to improve the efficiency of the 1p-DAB cannot be used in 3p-DAB applications directly. An enhanced modulation strategy is proposed for the 3p-DAB to address the problem of poor partial load efficiency in [19]. The proposed modulation strategy operates two phases in parallel at low and medium loads where the 3p-DAB is operated as a 1p-DAB that has high efficiencies with the triangular and trapezoidal current modes. PS control is still applied at high loads. However, the converter will lose the benefit of small ripple output current as a result of the noninterleaved operation. Additionally, it requires highly synchronized gate triggering circuits and changes the paralleled phases periodically, which increases the control complexity.

With the fixed PS angle among three phases, a new operating mode is introduced for the 3p-DAB in [20], where a constant duty cycle of 1/3 is employed for each phase leg. This operating mode fails to improve the converter performance in the whole load range and even causes low efficiencies for some operating points. A current-fed 3p-DAB converter as well as its optimized modulation strategy is proposed in [21]. The same variable duty cycle is applied for both the primary and the secondary bridges to maintain ZVS in the whole operating range in this literature. However, the current-fed 3p-DAB employs three large inductors that reduce the power density of the converter. A similar switching pattern is discussed in [22] and is defined as the simultaneous pulsewidth-modulation (SPWM) control. Seven different switching modes are introduced with overlapped ZVS ranges. This literature only analyzes the possible ZVS ranges of the 3p-DAB under SPWM and provides no solutions for the optimal control parameters. Three triangular and trapezoidal current modes for the 3p-DAB are introduced and analyzed in [23]. The proposed modulation strategy extends the soft-switching range and increases the light-load efficiency of the 3p-DAB. However, the mode selection and the computation of duty cycles are not further discussed. In addition, the triangular and trapezoidal current modes cannot cover the whole load range. It is expected that introducing the variable duty cycles for the active bridges is an effective approach to optimize the operation of the 3p-DAB. Actually, the previous modulation strategies can be considered as the special cases of this approach. Nevertheless, the operating principles of the 3p-DAB with variable duty cycles are not well addressed in the existing literature. Due to multiple degrees of freedom, it is considerably complex to determine the optimal control parameters with respect to the efficiency-optimized objective. There is not an effective procedure that determines the global optimal control parameters in the whole operating range at present. Consequently, no practical optimized modulation strategy is found for the 3p-DAB with variable duty cycles.

The dynamic behavior is another important issue for the optimized operation of the 3p-DAB. When the duty cycles (including the PS angle) change fast as a result of the abruptly changed transmission power, the transformer currents (also defined as the phase currents) have transient dc biases and become unbalanced, leading to the magnetic bias and oscillations in output currents. A similar transient process can be found in the 1p-DAB. Essentially, the transient dc bias of the transformer current is caused by the transient nonzero voltage–time product of the transformer voltage due to alternative duty cycles during a switching period. It is concluded for both 1p-DAB and 3p-DAB. In order to minimize the transient time, an asymmetric double-side modulation method is proposed, which enables the 1p-DAB to transfer from one steady state to another one smoothly [24]. A transient PS method with the same principle is developed in [25]. The predictive current control is proposed to achieve the optimum and robust dynamic response of the 1p-DAB in [26]. Since the current reference is achieved within one switching period, the transient dc bias is eliminated simultaneously. Nevertheless, an extra current sensor is required, which increases the cost of the converter. Two instantaneous current control methods are proposed for the 3p-DAB in [27] and [28]. By means of the intermediate PS angles, the proposed control methods enable the converter to reach new steady states in one-third of a switching period and half a switching period. All of these publications exist on the converter with PS control, while the dynamic control of the converter with variable duty cycles is seldom mentioned. In fact, multiple degrees of freedom will complicate the dynamic behaviors of the converter, but also provide more flexible approaches to improve the transient performance. Therefore, the dynamic behavior as well as the control method of the 3p-DAB with variable duty cycles becomes a practical issue that demands further investigations.

The duty cycle control (DCC), which provides three degrees of freedom including variable duty cycles for active bridges

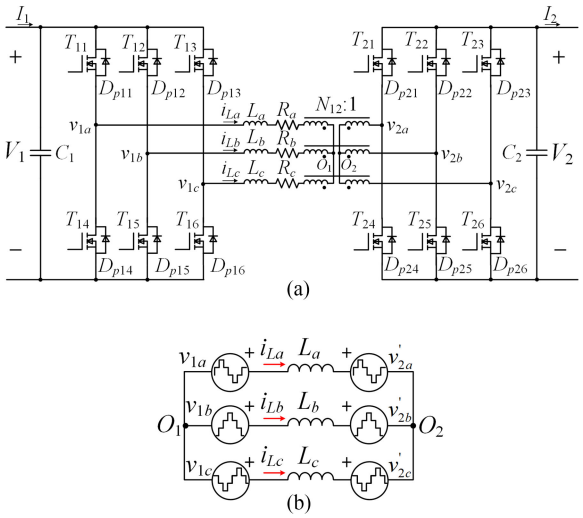

Fig. 1. Circuit schematic and equivalent circuit for the 3p-DAB. (a) Circuit schematic. (b) Equivalent circuit.

and the PS angle, is expected to optimize the operation of the 3p-DAB. This paper presents comprehensive analysis of DCC in a unified perspective. By applying the multifrequency approximation method, a precise and universal model is deduced for the 3p-DAB under DCC, which can be used to compute the analytic expressions of circuit variables regardless of numerous switching modes. On this basis, an optimized modulation strategy is proposed to minimize the conduction losses of the 3p-DAB in the whole load range. The optimal control parameters are obtained by employing an interior-point algorithm. The switching operation of the converter with the optimized modulation strategy is then analyzed, and it is concluded that the proposed modulation strategy extends the soft-switching range of the 3p-DAB simultaneously. Consequently, high efficiency is realized for the converter. This paper also presents detailed descriptions on the closed-loop control of the 3p-DAB under DCC. Moreover, the dynamic behavior of the 3p-DAB with variable duty cycles is investigated, and a fast transient current control (FTCC) method is proposed to improve the transient performance. The proposed control method enables the converter to transfer from one steady state to another within about one-third switching period, hence balancing the transformer currents rapidly and avoiding oscillations in dc currents. Since the discussions about the steady-state operation and the dynamic control are based on a unified analysis of DCC, a unified implement standard is developed for the 3p-DAB under DCC in this paper.

II. Duty Cycle Control of the 3p-DAB

A. Operating Principles

Fig. 1(a) illustrates the circuit schematic of the 3p-DAB converter. V_1 and V_2 are the dc voltages of active bridges. I_1 and I_2 are the port currents. C_1 and C_2 are the dc capacitors. L_a, L_b, and L_c are the equivalent series inductances including the leakage inductances of the transformer and the external inductors. R_a, R_b, and R_c are the equivalent series resistances consisting of the series resistances of the external inductors and the windings of the transformer. N_{12} is the primary to secondary turns ratio of the transformer. O_1 as well as O_2 denotes the neutral point. T_{xy} denotes the active switch, and D_{pxy} denotes the corresponding antiparallel diode, where $x = 1, 2$ and $y = 1, 2 \ldots 6$. i_{La}, i_{Lb}, and i_{Lc} are the phase currents in the V_1-side active bridge. Fig. 1(b) presents the equivalent circuit for the 3p-DAB, where v_{1x} and v'_{2x} $(= N_{12} v_{2x}, x = a, b, c)$ are equivalent ac phase voltages on the V_1 side.

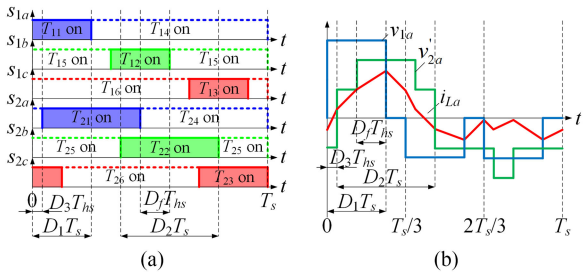

Fig. 2. Driving pulses and general operating waveforms for the 3p-DAB under DCC. (a) Driving pulses. (b) Operating waveforms.

In the equivalent circuit, the three-phase active bridge is equivalent to three step-wave ac voltage sources with Y connection. In practice, the value of the magnetizing inductance is usually much larger than that of the equivalent series inductance. Thus, the magnetizing inductances can be neglected, and the transformer is represented by the equivalent series inductances. The equivalent series resistances are also neglected due to their minimal influences on the steady-state analysis. In each phase, the phase voltages are connected through the series inductance. It is obvious that the three-phase topology is symmetrical. Without loss of generality, phase a is taken, for example, to analyze the converter in this paper.

The driving pulses for active switches and the general operating waveforms of the 3p-DAB under DCC are presented in Fig. 2. The three-phase legs of each active bridge are operated with a PS of $2\pi/3$ (or described as $T_s/3$ where T_s is the switching period). A variable duty cycle is employed for each phase leg. Three-phase legs in one active bridge have the same duty cycle. The PS between the active bridges is adjustable. As shown in Fig. 2(a), D_1 and D_2 denote the duty cycles for V_1-side and V_2-side bridges, respectively. The width of the driving pulse is denoted by $D_1 T_s$ or $D_2 T_s$. D_3 is the PS ratio between two active bridges, which is defined by the rising edges of the driving pulses. The PS angle is denoted by $D_3 T_{hs}$, where T_{hs} is the half-switching period. The value ranges of three control parameters are $0 \le D_1 \le 1$, $0 \le D_2 \le 1$, and $-1 \le D_3 \le 1$, where a positive D_3 indicates that the driving pulse for T_{11} leads that for T_{21}, and vice versa. The definition ensures that both the driving pulse and the PS angle have an interval length of T_s. Additionally, another PS ratio D_f is defined, which denotes the PS ratio between the centers of the driving pulses for the corresponding active switches such as T_{11} and T_{21}. The value of D_f is in the range of $[-1, 1]$ as well. From the following analysis, it can be concluded that D_f has a special meaning for the operation of the 3p-DAB. It is evident that the previous approaches are the special cases of DCC, as illustrated in Fig. 3 [6], [22],

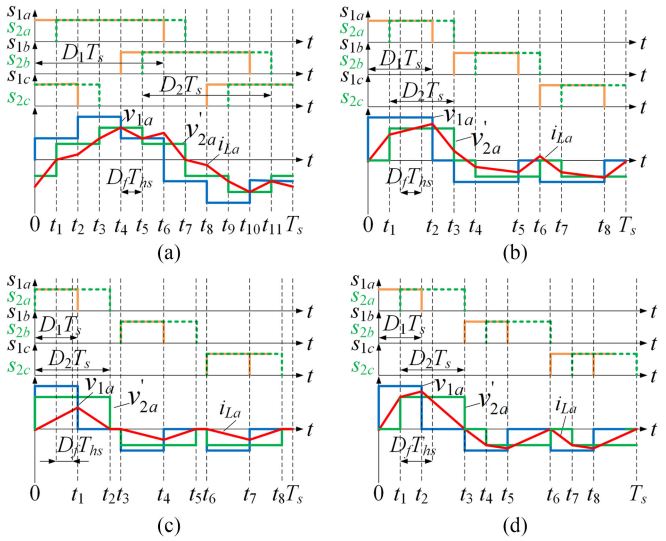

Fig. 3. Operating waveforms of the 3p-DAB under different modulation strategies. (a) PS control. (b) SPWM control. (c) Triangular current mode. (d) Trapezoidal current mode.

[23]. For example, PS control is applied when $D_1 = D_2 = 0.5$, and SPWM is applied when $0 \leq D_1 = D_2 \leq 1$.

To facilitate the analysis, the switching function $s(t)$ is introduced for each phase leg. A value of 1 indicates that the upper switch of the corresponding phase leg is ON and the lower switch is OFF, whereas 0 means that the upper switch is OFF and the lower switch is ON. According to the switching sequences and the definition of $s(t)$, the phase voltages on the V_1 side are derived as

$$\begin{cases} v_{1a}(t) = \dfrac{V_1\left[2s_{1a}(t) - s_{1b}(t) - s_{1c}(t)\right]}{3} \\ v_{1b}(t) = \dfrac{V_1\left[2s_{1b}(t) - s_{1a}(t) - s_{1c}(t)\right]}{3} \\ v_{1c}(t) = \dfrac{V_1\left[2s_{1c}(t) - s_{1a}(t) - s_{1b}(t)\right]}{3} \end{cases} \tag{1}$$

$$\begin{cases} v'_{2a}(t) = \dfrac{N_{12}V_2\left[2s_{2a}(t) - s_{2b}(t) - s_{2c}(t)\right]}{3} \\ v'_{2b}(t) = \dfrac{N_{12}V_2\left[2s_{2b}(t) - s_{2a}(t) - s_{2c}(t)\right]}{3} \\ v'_{2c}(t) = \dfrac{N_{12}V_2\left[2s_{2c}(t) - s_{2a}(t) - s_{2b}(t)\right]}{3} \end{cases} \tag{2}$$

where the subscripts of $s(t)$ denote the corresponding phase leg, e.g., $s_{1a}(t)$ is the switching function for phase a of the V_1-side active bridge. As shown in Fig. 2(b), the phase voltage is in an asymmetrical six-step mode. However, the volt-seconds over a complete switching period remain balanced. In order to simplify the analysis, the values of L_a, L_b, and L_c are all equal to L_s. From the equivalent circuit, the phase current i_{La} in phase a is obtained as

$$i_{La}(t) = i_{La}(0) + \frac{1}{L_s}\int_0^t \left[v_{1a}(\rho) - v'_{2a}(\rho)\right] d\rho \tag{3}$$

where ρ is used to denote the time within a period. Furthermore, the basic electrical quantities of the 3p-DAB can be derived based on the equivalent circuit. The root mean square (rms) phase current and the average transmission power of phase a are given by

$$I_{Larms} = \sqrt{\frac{1}{T_s}\int_0^{T_s} i_{La}^2(t)\, dt}, \tag{4}$$

$$P_a = \frac{1}{T_s}\int_0^{T_s} v_{1a}(t)\, i_{La}(t)\, dt. \tag{5}$$

Assuming that the corresponding circuit parameters of three phases are equal, the rms phase current for each phase and the total transmission power (or defined as the output power) of three phases are expressed as

$$I_{Lrms} = I_{Larms} = I_{Lbrms} = I_{Lcrms}, \tag{6}$$

$$P_o = 3P_a = \frac{3}{T_s}\int_0^{T_s} v_{1a}(t)\, i_{La}(t)\, dt. \tag{7}$$

B. Generalized Analysis of the 3p-DAB Under DCC

Under PS control, both active bridges of the 3p-DAB are operated in the six-step mode since the phase voltage and current have odd symmetry at every half-switching period [6]. Two switching modes are distinguished by regarding the different sequences of rising and falling slopes of the phase current, which is expressed by a piecewise function. The switching modes are analyzed by using the piecewise linear method. However, this method is not effective for the 3p-DAB under DCC due to numerous switching modes. To overcome this issue, the multifrequency approximation is applied to analyze the operation of the 3p-DAB. A universal steady-state model is developed to describe the analytical expressions for the high-frequency-link electrical quantities of the 3p-DAB under DCC. Thus, analysis of numerous switching modes is avoided. The universal expression for the switching function is given by

$$s(t) = \begin{cases} 1, & t_0 < t \leq t_0 + DT_s \\ 0, & 0 \leq t \leq t_0 \text{ or } t_0 + DT_s < t \leq T_s \end{cases} \tag{8}$$

where t_0 is the initial time of driving pulse for the upper active switch and D denotes the duty cycle. By substituting the Fourier series of switching functions into (1) and (2), v_{1a} and v'_{2a} are expressed as

$$v_{1a}(t) = \sum_{k=1}^{+\infty} \frac{8V_1 \sin^2\left(\frac{k\pi}{3}\right)\sin(kD_1\pi)\cos(k\omega_s t - kD_1\pi)}{3k\pi} \tag{9}$$

$$v'_{2a}(t) = \sum_{k=1}^{+\infty} \frac{8N_{12}V_2 \sin^2\left(\frac{k\pi}{3}\right)\sin(kD_2\pi)\cos\begin{pmatrix} k\omega_s t - kD_1\pi \\ -kD_f\pi \end{pmatrix}}{3k\pi} \tag{10}$$

where the angular frequency $\omega_s = 2\pi/T_s$, and the initial time of driving pulse for T_{11} is defined as zero time. It is observed

that D_f is also the PS ratio between $v_{1a(1)}$ and $v'_{2a(1)}$, where $v_{1a(1)}$ and $v'_{2a(1)}$ are defined as the fundamental components of v_{1a} and v'_{2a}, respectively. By combining (3), (9), and (10), the expression for the phase current can be derived. Since the volt-seconds over a complete switching period are balanced, the average phase current over one switching period should be zero. On this basis, $i_{La}(0)$ is calculated. Then, substituting $i_{La}(0)$ into (3), the phase current is obtained as

$$i_{Lan}(t) = \frac{i_{La}}{I_b} = \sum_{k=1}^{+\infty} A(k) \frac{\sin(k\omega_s t - kD_1\pi)}{k} - \sum_{k=1}^{+\infty} B(k) \frac{\sin(k\omega_s t - kD_1\pi - kD_f\pi)}{k} \quad (11)$$

where

$$A(k) = \frac{8\sin^2(k\pi/3)\sin(kD_1\pi)}{3k\pi}$$

$$B(k) = \frac{8d\sin^2(k\pi/3)\sin(kD_2\pi)}{3k\pi}$$

the reference current I_b is $V_1/(\omega_s L_s)$, and the voltage conversion ratio d is defined as $N_{12}V_2/V_1$. Furthermore, the normalized rms phase current and the normalized total average transmission power are derived as (12) and (13) as shown at the bottom of this page, where the reference power P_b is $V_1^2/(\omega_s L_s)$. It can be deduced from (13) that the direction of transmission power is solely determined by the sign of D_f. Similar to the conventional 3p-DAB operation, a positive D_f leads to the power transfer from V_1 port to V_2 port, whereas a negative D_f leads to the power transfer in the reverse direction. By combining (11)–(13), it can be further concluded that the forward-power-transfer operation and the corresponding reverse-power-transfer operation share the same duty cycles but opposite D_f. Hence, analysis of the forward-power-transfer operation is enough

III. Minimum-Conduction-Loss Modulation of 3p-DAB Converters

The three degrees of freedom (D_1, D_2, and D_f) have infinite combinations to transfer the required power with the required voltage conversion ratio. On the basis of DCC, this section proposes an optimized modulation strategy to minimize the conduction losses with the required transmission power and voltage conversion ratio in the whole load range. To simplify the analysis, the discussion assumes that the power flow is from V_1 port to V_2 port ($D_f \geq 0$) in a buck mode ($d < 1$). The other working cases can be analyzed similarly.

A. Optimized Modulation Strategy to Minimize the Conduction Losses in the Whole Load Range

The calculation of conduction losses considers two parts: the conduction losses in switches and the copper losses in magnetic elements. The rms currents through the switches and the transformer determine the respective conduction losses. It should be pointed out that the switch consists of the active switch and the corresponding antiparallel diode. The detailed derivation of the conduction losses in the 1p-DAB is found in [17]. Accordingly, a similar derivation can be applied for the 3p-DAB. It can also be concluded that the conduction and copper losses are directly proportional to I_{Lrms}^2. Consequently, the minimum rms phase current leads to the minimum conduction losses.

Based on the aforementioned analysis, the conduction losses are considered as the optimized objective that improves the operation of the 3p-DAB herein. The optimization problem can be described as finding optimal control parameters for minimizing the rms phase current with the required transmission power and voltage conversion ratio. Therefore, the numerical optimization problem with a single objective can be formulated into a constrained nonlinear programming model as

$$\begin{aligned} &\text{Min } I_{L\text{rmsn}}(\boldsymbol{X}), \\ &\text{Subject to} \\ &P_{on}(\boldsymbol{X}) - P_{onref} = 0,\ B_j(\boldsymbol{X}) \leq 0,\ j = 1, 2, \ldots 6 \end{aligned} \quad (14)$$

where $\boldsymbol{X} = (D_1, D_2, D_f)$, $I_{Lrmsn}(\boldsymbol{X})$ and $P_{on}(\boldsymbol{X})$ are given by (12) and (13), respectively, P_{onref} is the required transmission power, and $B_j(\boldsymbol{X})$ are determined by the operational constraints of three control parameters that

$$B_1(\boldsymbol{X}) = -D_1,\ B_2(\boldsymbol{X}) = D_1 - 1,\ B_3(\boldsymbol{X}) = -D_2,$$
$$B_4(\boldsymbol{X}) = D_2 - 1,\ B_5(\boldsymbol{X}) = -D_f, \text{ and } B_6(\boldsymbol{X}) = D_f - 1.$$

In the constrained nonlinear programming model, $I_{L\text{rmsn}}(\boldsymbol{X})$ is the single objective function, $P_{on}(\boldsymbol{X}) - P_{onref}$ is the equality constraint, and $B_j(\boldsymbol{X})$ ($j = 1, 2, \ldots, 6$) are inequality constraints. However, it is difficult to derive the closed-form solutions for three control parameters in practice. To overcome this issue, an interior point algorithm is applied to solve the numerical optimization problem and compute the numerical optimal control parameters.

Interior point methods (also referred to as barrier methods) are a certain class of algorithms that solve linear and nonlinear convex optimization problems [29], [30]. In the interior point method, the logarithmic barrier functions are introduced to approximately formulate the optimization problem in the form of an equality constrained problem. Thus, the constrained

$$I_{L\text{rmsn}} = \frac{I_{Lrms}}{I_b} = \sqrt{\sum_{k=1}^{+\infty} \frac{32\sin^4\left(\frac{k\pi}{3}\right)\left[\sin^2(kD_1\pi) + d^2\sin^2(kD_2\pi) - 2d\sin(kD_1\pi)\sin(kD_2\pi)\cos(kD_f\pi)\right]}{9k^4\pi^2}} \quad (12)$$

$$P_{on} = \frac{P_o}{P_b} = \sum_{k=1}^{+\infty} \frac{32d\sin^4\left(\frac{k\pi}{3}\right)\sin(kD_1\pi)\sin(kD_2\pi)\sin(kD_f\pi)}{3k^3\pi^2} \quad (13)$$

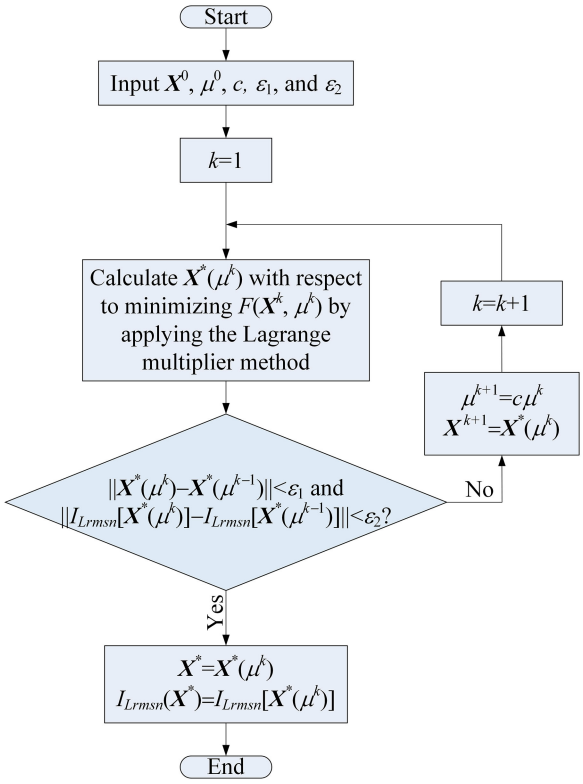

Fig. 4. Simplified flowchart of the optimization algorithm based on an interior point method.

nonlinear programming model is given by

$$\text{Min } F(\boldsymbol{X},\mu) = I_{Lrmsn}(\boldsymbol{X}) - \mu\sum_{i=1}^{6}\ln\sigma_i,$$

$$\begin{aligned}\text{Subject to } & P_{on}(\boldsymbol{X}) - P_{onref} = 0,\ -D_1 + \sigma_1 = 0,\\ & D_1 - 1 + \sigma_2 = 0,\ -D_2 + \sigma_3 = 0,\ D_2 - 1 + \sigma_4 = 0,\\ & -D_f + \sigma_5 = 0,\ D_f - 1 + \sigma_6 = 0 \end{aligned} \quad (15)$$

where $\mu > 0$ is the barrier parameter, and $\sigma_i > 0$ is the slack variable. In the interior-point method, the algorithm starts from an initial point within the feasible domain and obtains a new interior point for minimizing the objective function along a feasible direction. It should be pointed out that since the nonlinear programming model only contains equality constraints, the Lagrange multiplier method can be directly applied to solve the optimization problem. The algorithm then proceeds from the new interior point and derives the subsequent optimal interior point by an iterative operation along a feasible direction. After multiple iterations, a sequence of interior points is obtained, and the value of the objective function gradually tends to the optimal one. The simplified flowchart of the optimization algorithm based on an interior point method is illustrated in Fig. 4, where the superscript k indicates the value in the kth iteration, $\boldsymbol{X}^*$ denotes the optimal solution, $c < 1$ is the reduction coefficient, and ε_1 as well as ε_2 is the tolerance.

By using the optimization algorithm mentioned above, the global minimum rms phase current with the required transmission power and voltage conversion ratio can be derived. Meanwhile, the optimal control parameters are obtained, which are the optimal interior point after multiple iterations in practice. Fig. 5 depicts the calculated optimal control parameters, where $d = 0.6$ and 0.8 are taken as the example voltage conversion ratios for the two-dimensional curves. It can be observed that three optimal control parameters vary with P_{on} and d, distinguished from the conventional operation with constant duty cycles. Additionally, the numerical optimization algorithm selects $D_1 = D_2 = 0.5$ at high power levels, where PS control, as a special case of DCC, is applied actually. On the basis, the minimum-conduction-loss modulation strategy is proposed for the 3p-DAB, which minimizes the rms phase current as well as conduction losses in the whole load range. Fig. 6 compares the calculated rms phase currents of PS control and the optimized modulation scheme varied with P_{on} and d. It is evident that the proposed modulation strategy leads to lower rms phase current in most load range, especially with large voltage variations under light load conditions. As a consequence, lower conduction losses and higher efficiency are achieved for the 3p-DAB with the optimized modulation strategy.

B. Switching Characteristics of the 3p-DAB With the Optimized Modulation Strategy

The 3p-DAB converter provides inherent ZVS capability without adding any extra passive components and is particularly attractive for high-speed switching structures. However, ZVS operation of the 3p-DAB depends on the voltage conversion ratio and transmission power. Therefore, accurate identification of ZVS boundaries for switching modes is essential to precisely quantify the performance of the 3p-DAB throughout its entire operating range. ZVS is obtained by ensuring that the active switch turn-ON only occurs when its antiparallel diode is conducting. Then, the voltage across active switch is clamped to zero, and the current commutates to the active switch simultaneously. Consequently, the ZVS operation of active switch can be determined by the current flowing through the switch when turn-ON occurs. Since the currents flowing through the switches are corresponding to the phase current, ZVS constraints for all active switches can be uniformly given by the phase current. The typical approach to define ZVS boundaries for a 3p-DAB is to create piecewise time-based current definitions for the phase current and to solve these expressions in the time domain to identify whether the ZVS operation is realized. But for the 3p-DAB under DCC, it is quite difficult to apply this approach because of numerous switching modes. Based on the harmonic component analysis method [13], this paper presents an approach to determine ZVS boundaries of the 3p-DAB under all operating conditions.

Because the three-phase topology is symmetrical and three phases are operated with a PS of $T_s/3$, three phases have the same switching characteristic. Thus, the discussion on switching characteristics of phase a is enough. As depicted in Fig. 2, the initial time of the turn-ON signal for T_{11} is defined as zero time here. According to the definition of duty cycles, it can be obtained that the turn-ON signals for active switches in phase a

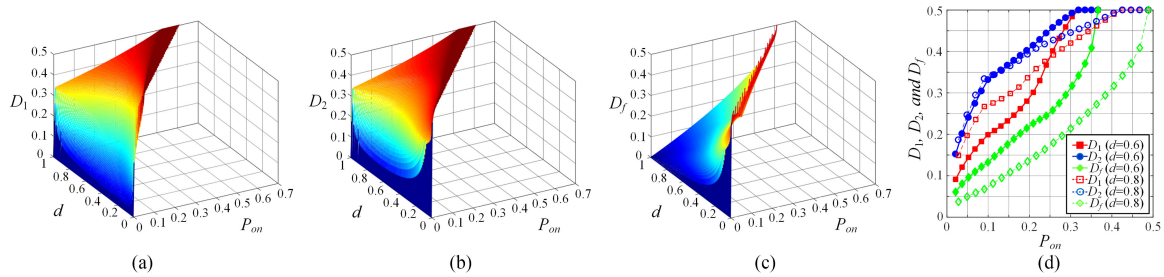

Fig. 5. Optimal control parameters with the required transmission power and voltage conversion ratio. (a) D_1. (b) D_2. (c) D_f. (d) Two-dimensional curves.

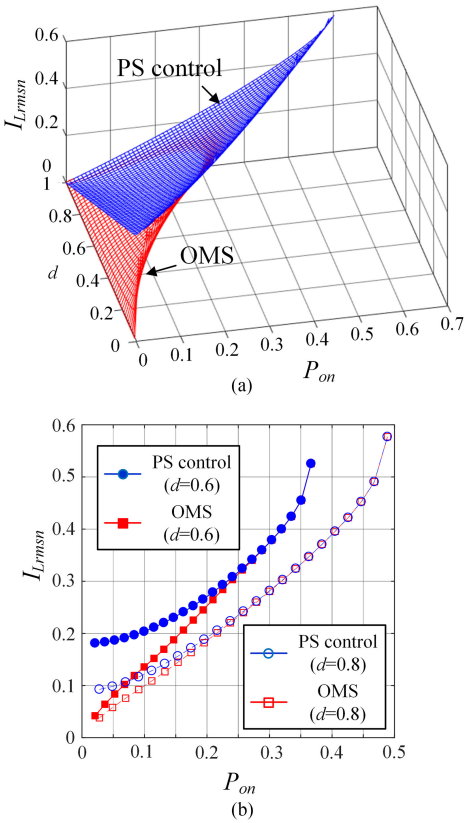

Fig. 6. Comparison of rms currents calculated from PS control and the optimized modulation strategy (OMS) with the required P_{on} and d. (a) Three-dimensional curves. (b) Two-dimensional curves.

(i.e., T_{14}, T_{21}, and T_{24}) are then activated at $t = D_1T_s$, D_3T_{hs}, and $D_2T_s + D_3T_{hs}$, respectively. The other switch in the same leg is controlled complementarily. By substituting D_f for D_3, the initial time of the turn-ON signal for each active switch can be expressed as

$$\begin{aligned} t_0 &= 0, T_{11} \text{ on}, \\ t_1 &= D_1T_s, T_{14} \text{ on}, \\ t_2 &= \frac{D_1T_s}{2} - \frac{D_2T_s}{2} + \frac{D_fT_s}{2}, T_{21} \text{ on}, \\ t_3 &= \frac{D_1T_s}{2} + \frac{D_2T_s}{2} + \frac{D_fT_s}{2}, T_{24} \text{ on}. \end{aligned} \tag{16}$$

To ensure ZVS of both bridges, the phase current has to lag the ac voltage of the input bridge (V_1 side) while leading the ac voltage of the output bridge (V_2 side). This yields to the ZVS constraints of the 3p-DAB, which are as follows:

$$\begin{aligned} &i_{Lan}(t_0) < 0, \quad T_{11} \text{ on} \\ &i_{Lan}(t_1) > 0, \quad T_{14} \text{ on} \\ &i_{Lan}(t_2) > 0, \quad T_{21} \text{ on} \\ &i_{Lan}(t_3) < 0, \quad T_{24} \text{ on}. \end{aligned} \tag{17}$$

By combining (11), (16), and (17), the ZVS constraints are further derived as

$$\begin{aligned} &-\sum_{k=1}^{+\infty} A(k)\frac{\sin(kD_1\pi)}{k} + \sum_{k=1}^{+\infty} B(k)\frac{\sin(kD_1\pi + kD_f\pi)}{k} < 0, \\ &\qquad T_{11} \text{ on} \\ &\sum_{k=1}^{+\infty} A(k)\frac{\sin(kD_1\pi)}{k} - \sum_{k=1}^{+\infty} B(k)\frac{\sin(kD_1\pi - kD_f\pi)}{k} > 0, \\ &\qquad T_{14} \text{ on} \\ &-\sum_{k=1}^{+\infty} A(k)\frac{\sin(kD_2\pi - kD_f\pi)}{k} + \sum_{k=1}^{+\infty} B(k)\frac{\sin(kD_2\pi)}{k} > 0, \\ &\qquad T_{21} \text{ on} \\ &\sum_{k=1}^{+\infty} A(k)\frac{\sin(kD_2\pi + kD_f\pi)}{k} - \sum_{k=1}^{+\infty} B(k)\frac{\sin(kD_2\pi)}{k} < 0, \\ &\qquad T_{24} \text{ on}. \end{aligned} \tag{18}$$

By substituting the calculated optimal control parameters into the ZVS constraints, the ZVS operation of the 3p-DAB with the optimized modulation strategy is investigated. Together with (13), the ZVS boundaries in the diagram of the transmission power with respect to the voltage conversion ratio are determined. Fig. 7 illustrates the ZVS boundaries of the 3p-DAB under PS control and the optimized modulation strategy. It is evident that PS control does not allow the soft-switching operation at low loads when the voltage conversion ratio is away from unity. As depicted in Fig. 7, the optimized modulation strategy extends the ZVS range of the 3p-DAB, especially at large voltage variations. Nevertheless, full ZVS operation is not effective in the whole load range, while some active switches realize zero-current switching (ZCS) at low loads.

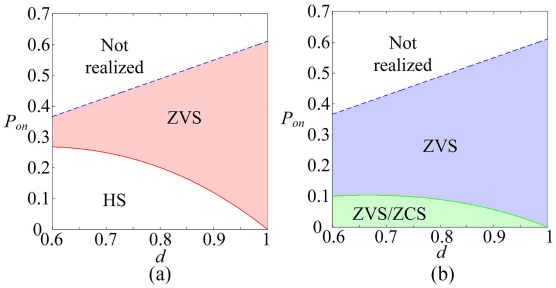

Fig. 7. Comparison of the soft-switching ranges with PS control and the optimized modulation strategy. (a) PS control. (b) Optimized modulation strategy.

Based on the inspection of numerous calculated optimal control parameters, it has been found that the triangular current mode yields the minimum rms phase current at low loads. Fig. 3(c) illustrates the driving pulses and typical operating waveforms for phase a of the 3p-DAB with the triangular current mode, where the shape of phase current is triangular during $0 < t < t_2$, $t_3 < t < t_5$, and $t_6 < t < t_8$, and the phase current is zero during the subintervals of $t_2 < t < t_3$, $t_5 < t < t_6$, and $t_8 < t < T_s$. As depicted in Fig. 3(c), T_{14} and T_{24} are turned OFF, while T_{11} and T_{21} are turned ON at zero time. D_3 is equal to zero in this switching mode. It is evident that the active switches are turned ON/OFF at ZCS as $i_{La}(0)$ is equal to zero. At t_1, T_{11} is turned OFF and T_{14} is turned ON. As $i_{La}(t_1) > 0$, the current flows through D_{14} after the commutation ends. Therefore, T_{14} is turned ON at ZVS. At t_2, T_{21} is turned OFF and T_{24} is turned ON. That is, $i_{La}(t_2) = 0$ ensures ZCS operations for T_{21} and T_{24}. Consequently, the triangular current mode realizes full soft-switching operation for the 3p-DAB under the light load conditions.

The duration of the freewheeling time intervals (i.e., $[t_2, t_3]$, $[t_5, t_6]$, and $[t_8, T_s]$) decreases with the increasing output power. The duration becomes zero at the maximum output power of the triangular current mode. It can be concluded that the transition from the ZVS/ZCS operation range to the ZVS operation range is continuous. Thus, the soft-switching boundaries of the switching modes used in the optimized modulation strategy are naturally connected, as shown in Fig. 7. In summary, the proposed minimum-conduction-loss modulation strategy extends the soft-switching range of the 3p-DAB simultaneously. Therefore, the proposed modulation strategy is expected to boost the efficiency of the 3p-DAB, especially at low loads.

C. Closed-Loop Control of the 3p-DAB Under DCC

In order to operate the 3p-DAB converter under DCC in a closed loop, a typical control strategy is developed, and the structure schematic is illustrated in Fig. 8. The discussion assumes that the power flow is from V_1 port to V_2 port; hence, the output voltage V_2 is controlled. In the closed loop, a PI controller regulates the PS ratio D_f to generate the set output, and the modulator determines the duty cycles D_1 and D_2 to improve the performance of the 3p-DAB. The dc voltages and output current, i.e., V_1, V_2, and I_2, are measured, while digital moving average filters are applied to remove noise. The duty

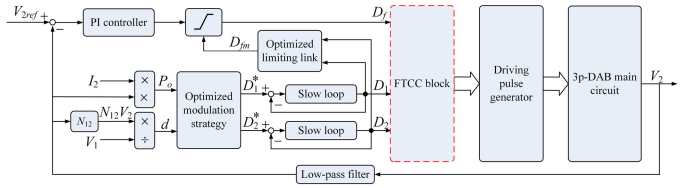

Fig. 8. Structure schematic of the closed-loop control strategy.

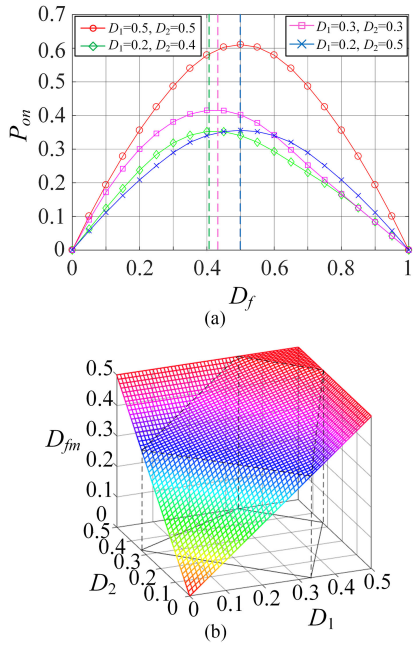

Fig. 9. Transmission power and optimal saturation limits with variable D_1 and D_2. (a) P_{on}. (b) D_{fm}.

cycles with respect to the required transmission power P_o and voltage conversion ratio d are calculated according to the optimized modulation strategy. In practice, the desired optimal duty cycles D_1^* and D_2^* are calculated off-line and prestored in the memory of a microcontroller. Then, D_1^* and D_2^* are obtained on-line by using the method of a lookup table. On this base, the duty cycle calculation is accomplished with slow control loops that regulate D_1 and D_2 to the desired values. The slow loops are composed of large-inertia links or integration links with a large time constant, which realize the decoupling of three control parameters. The FTCC block indicates the fast transient current control that will be discussed in the next section. Subsequently, the driving pulse generator determines when to activate turn-ON signals of switches according to the duty cycles.

Generally, the conventional PI controller is a linear controller and a saturation limit is set to restrict the output. As D_f is the output of the PI controller here, the upper limit of D_f (i.e., 0.5) is considered as the saturation limit of the PI controller as usual. However, this setting works well for PS control, while may react poorly for DCC. According to (13), the curves of the transmission power with different duty cycles (D_1 and D_2) are illustrated in Fig. 9(a). It is evident that a constant limit 0.5 can be set for PS control because P_{on} increases monotonically when $D_f \leq 0.5$. Nevertheless, the PS ratio D_{fm} that produces the

maximum transmission power varies with different duty cycles and is not equal to 0.5 anymore. When $D_{fm} \leq D_f \leq 0.5$, P_{on} decreases monotonically. Thus, the constant limit 0.5 is not appropriate for the PI controlled 3p-DAB with variable duty cycles. This setting will slow down the dynamic response, and even cause the converter to fail in achieving the control target. In order to solve this problem, the saturation limit should be updated with respect to the duty cycles. Based on (13), the values of D_{fm} under different D_1 and D_2 can be calculated, as depicted in Fig. 9(b). By inspecting the numerical results, the closed-form solutions of D_{fm} can be further summarized as (19) as shown at the bottom of the page.

As shown in Fig. 8, an optimized limiting link based on (19) is introduced into the closed-loop control blocks. This link ensures that the current saturation limit is set as D_{fm} with respect to the required duty cycles. Consequently, the dynamic response is guaranteed, and the system is more stable as well.

IV. Fast Transient Current Control for the 3p-DAB With Variable Duty Cycles

When the duty cycles (including the PS ratio) change fast as a result of the abruptly changed transmission power, the transformer currents have transient dc biases and become unbalanced, leading to the magnetic bias and oscillations in output currents. This section presents a detailed description of the dynamic behavior of the 3p-DAB with variable duty cycles. On this basis, an FTCC method is proposed to improve the transient performance.

A. Conventional Method

The initial steady states of the control parameters are assumed to be $(D_{1,1}, D_{2,1}, D_{f,1})$. As a result of the changed transmission power, the target steady states of the control parameters are denoted by $(D_{1,2}, D_{2,2}, D_{f,2})$. In the conventional method, the target control parameters will be loaded to the register immediately, and the corresponding driving pulses are expected in the next switching period. The loading time can be any time in the switching period. Usually, the rising edge or the center of the driving pulse is chosen as the loading time, which helps to generate the loading signal in the digital signal processor (DSP). Fig. 10 shows the waveforms of the switching functions, voltages, and phase currents with the conventional method. Herein, the calibration of the transverse-axis is given by the radian $\theta\,(=\omega_s t)$.

Two cases are studied, where the loading time is the rising edge of driving pulse for T_{11} in Fig. 10(a), and that is the center of driving pulse for T_{11} in Fig. 10(c). It is evident that the switching functions change asymmetrically in two cases,

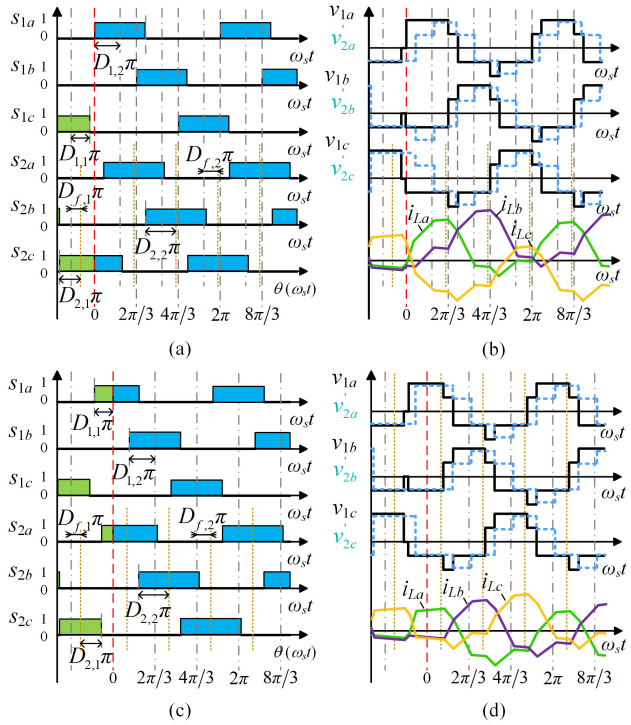

Fig. 10. Waveforms of switching functions, voltages, and phase currents with the conventional method. (a) Switching functions. (b) Operating waveforms. (c) Switching functions. (d) Operating waveforms.

resulting in the unbalanced phase currents. As depicted in Fig. 10(a), the pulsewidth of s_{1a} is $(D_{1,1} + D_{1,2})\pi$ during a switching period, while that of s_{1b} and s_{1c} is $2D_{1,2}\pi$. Consequently, the transient nonzero voltage–time product arises. This will lead to transient dc biases in the phase currents. A similar phenomenon can be observed in Fig. 10(c). If so, the nonzero dc component of the phase current would result in the saturation of the transformer. However, the dc biases will be eliminated due to the nonzero resistance. Actually, the envelope of the phase current waveform would shift down with the time constant until the average phase current becomes zero. The settling time of the transient depends on the value of the resistance. On the other hand, a low resistance is preferred for reducing the conduction losses, which is against shortening the transient process. Therefore, an optimized current control method is required to improve the transient performance of the 3p-DAB under DCC.

B. Operating Principles of FTCC for the 3p-DAB Under DCC

In order to solve the aforementioned issue, an effective approach is involving two intermediate duty cycles in two different phases of the three-phase bridge during one-third switching period. The intermediate duty cycles are estimated for ensuring

$$D_{fm} = \begin{cases} D_1 + D_2, & D_1 + D_2 < 1/3, \\ D_2, & 2D_2 - D_1 > 2/3,\ D_2 < 1/2, \\ D_1, & 2D_1 - D_2 > 2/3,\ D_1 < 1/2, \\ 1/2, & D_1 + D_2 > 5/6,\ D_1 < 1/2, D_2 < 1/2, \\ (3D_1 + 3D_2 + 2)/9, & 1/3 < D_1 + D_2 < 5/6,\ 2D_2 - D_1 < 2/3,\ 2D_1 - D_2 < 2/3 \end{cases} \tag{19}$$

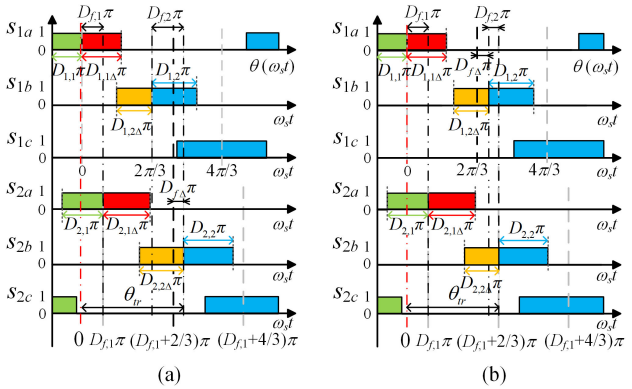

Fig. 11. Waveforms of the switching functions during the transient process under FTCC. (a) Case I. (b) Case II.

that the current achieves the steady state with $(D_{1,2}, D_{2,2}, D_{f,2})$ in about one-third period, thereby balancing the currents rapidly. On this basis, the FTCC method is proposed. Fig. 11 illustrates the switching functions during the transient process under FTCC. The intermediate duty cycles $D_{1,1\Delta}$ and $D_{1,2\Delta}$ are applied in the primary bridge, while the intermediate duty cycles $D_{2,1\Delta}$ and $D_{2,2\Delta}$ are applied in the secondary bridge. θ_{tr} denotes the transient interval when the control parameters change from $(D_{1,1}, D_{2,1}, D_{f,1})$ to $(D_{1,2}, D_{2,2}, D_{f,2})$. In order to facilitate distinction, the range where the control parameters are $(D_{1,1}, D_{2,1}, D_{f,1})$ is filled with green, the range where the control parameters are $(D_{1,2}, D_{2,2}, D_{f,2})$ is filled with blue, the range where the intermediate duty cycles $D_{1,1\Delta}$ and $D_{2,1\Delta}$ are used is filled with red, and the range where the intermediate duty cycles $D_{1,2\Delta}$ and $D_{2,2\Delta}$ are used is filled with orange. As shown in Fig. 11, two basic cases are distinguished according to the difference $D_{f\Delta}$ that is defined as $D_{f,2} - D_{f,1}$. Detailed analysis of two cases and operating principles of FTCC are presented as follows.

Case I: $D_{f\Delta} \geq 0$

As depicted in Fig. 11(a), the center of the driving pulse for T_{11} is defined as zero time. For the V_1-side bridge, the switching functions are in the steady state with $D_1 = D_{1,1}$ before zero time. Then, the switching functions enter the transient process at $\theta = 0$, when $D_{1,1\Delta}$ is loaded for s_{1a}, and $D_{1,2\Delta}$ is loaded for s_{1b}. At $\theta = 2\pi/3$, $D_{1,2}$ is loaded for s_{1a}, s_{1b}, and s_{1c}, and the transient process ends. The resulting waveforms of s_{1a}, s_{1b}, and s_{1c} are illustrated in Fig. 11(a), from which the values of three switching functions in [0, $2\pi/3$] are easy to get. Table I summarizes the function values and the corresponding time ranges. For the V_2-side bridge, the switching functions are in the steady state with $D_2 = D_{2,1}$ before $\theta = D_{f,1}\pi$. Then, the switching functions enter the transient process at $\theta = D_{f,1}\pi$, when $D_{2,1\Delta}$ is loaded for s_{2a}, $D_{2,2\Delta}$ is loaded for s_{2b}, and meanwhile s_{2b} as well as s_{2c} is shifted with $D_{f,2}\pi$. At $\theta = 2\pi/3 + D_{f,2}\pi$, $D_{2,2}$ plus $D_{f,2}$ is loaded for s_{2a}, s_{2b}, and s_{2c}, and the transient process ends. Table I summarizes the function values and the corresponding time ranges of s_{2a}, s_{2b}, and s_{2c} in $[D_{f,1}\pi, 2\pi/3 + D_{f,2}\pi]$.

In case I, two intermediate duty cycles $D_{1,1\Delta}$ and $D_{1,2\Delta}$ are introduced for the V_1-side bridge, and the transient process lasts for $2\pi/3$. For the V_2-side bridge, not only are the intermediate duty cycles $D_{2,1\Delta}$ and $D_{2,2\Delta}$ introduced, but the target PS ratio $D_{f,2}$ is loaded in the transient process. As a result, the corresponding transient process lasts for $2\pi/3 + D_{f\Delta}\pi$.

Case II: $D_{f\Delta} < 0$

For case II, a similar analysis is made. As depicted in Fig. 11(b), For the V_1-side bridge, the switching functions are in the steady state with $D_1 = D_{1,1}$ before zero time. Then, the switching functions enter the transient process at $\theta = 0$, when $D_{1,1\Delta}$ is loaded for s_{1a}, $D_{1,2\Delta}$ is loaded for s_{1b}, and meanwhile s_{1b} as well as s_{1c} is shifted with $|D_{f\Delta}\pi|$. At $\theta = 2\pi/3 + |D_{f\Delta}\pi|$, $D_{1,2}$ plus $|D_{f\Delta}\pi|$ is loaded for s_{1a}, s_{1b}, and s_{1c}, and the transient process ends. Table I summarizes the function values and the corresponding time ranges of s_{1a}, s_{1b}, and s_{1c} in $[0, 2\pi/3 + |D_{f\Delta}\pi|]$. For the V_2-side bridge, the switching functions are in the steady state with $D_2 = D_{2,1}$ before $\theta = D_{f,1}\pi$. Then, the switching functions enter the transient process at $\theta = D_{f,1}\pi$, when $D_{2,1\Delta}$ is loaded for s_{2a}, and $D_{2,2\Delta}$ is loaded for s_{2b}. At $\theta = 2\pi/3 + D_{f,1}\pi$, $D_{2,2}$ is loaded for s_{2a}, s_{2b}, and s_{2c}, and the transient process ends. The function values and the corresponding time ranges of s_{2a}, s_{2b}, and s_{2c} in $[D_{f,1}\pi, 2\pi/3 + D_{f,1}\pi]$ can also be found in Table I.

It is obvious that the operations of two cases are dual. In case II, not only are the intermediate duty cycles $D_{1,1\Delta}$ and $D_{1,2\Delta}$ introduced for the V_1-side bridge, but the target PS ratio $D_{f,2}$ included in $D_{f\Delta}$ is loaded in the transient process. As a result, the corresponding transient process lasts for $2\pi/3 + |D_{f\Delta}\pi|$. For the V_2-side bridge, two intermediate duty cycles $D_{2,1\Delta}$ and $D_{2,2\Delta}$ are introduced, and the transient process lasts for $2\pi/3$.

C. Derivation for the Intermediate Duty Cycles

Under FTCC, the phase current is expected to achieve the new steady state when the transient process ends. On this condition, the intermediate duty cycles can be calculated. For the sake of economizing space, the circuit analysis of the 3p-DAB with variable duty cycles in $\alpha\beta$ coordinates and the calculation of the phase currents in the steady state are presented in the Appendix. The results are used directly here. Since the operations of two cases are dual as mentioned before, case I is taken as an example for deriving the intermediate duty cycles. For the V_1-side bridge, the transient process starts at $\theta = 0$ and ends at $\theta = 2\pi/3$. During the transient process, $D_{1,1\Delta}$ is loaded for s_{1a}, and $D_{1,2\Delta}$ is loaded for s_{1b}. By referring to Table I, (A-10), and (A-11), the current vectors of phases a and b at $\theta = 2\pi/3$ are obtained as

$$\begin{aligned}\vec{i}_{L1a}\left(\frac{2\pi}{3}\right) &= I_{eq1}e^{j0^\circ}\cdot\kappa\cdot\left(\Phi\left(D_{1,1\Delta}\right)-1\right)+\kappa\cdot\vec{i}_{L1a}\left(0\right),\\ \vec{i}_{L1b}\left(\frac{2\pi}{3}\right) &= I_{eq1}e^{j120^\circ}\cdot\left(1-\Phi\left(-D_{1,2\Delta}\right)\right)+\kappa\cdot\vec{i}_{L1b}\left(0\right).\end{aligned} \tag{20}$$

The value of s_{1c} is 0 during the transient process; hence, the current vector is expressed by (A-12). By substituting (20) and (A-12) into (A-6), the resulting current in subcircuit I (as

TABLE I
FUNCTION VALUES AND CORRESPONDING TIME RANGES OF SWITCHING FUNCTIONS UNDER FTCC

Switching function	Case	Time range for "s=1"	Time range for "s=0"
s_{1a}	I	$\left[0,\ D_{1,1\Delta}\pi\right]$	$\left(D_{1,1\Delta}\pi,\ 2\pi/3\right]$
	II	$\left[0,\ D_{1,1\Delta}\pi\right]$	$\left(D_{1,1\Delta}\pi,\ 2\pi/3+\left\|D_{f\Delta}\pi\right\|\right]$
s_{1b}	I	$\left(2\pi/3-D_{1,2\Delta}\pi,\ 2\pi/3\right]$	$\left[0,\ 2\pi/3-D_{1,2\Delta}\pi\right]$
	II	$\left(2\pi/3+\left\|D_{f\Delta}\pi\right\|-D_{1,2\Delta}\pi,\ 2\pi/3+\left\|D_{f\Delta}\pi\right\|\right]$	$\left[0,\ 2\pi/3+\left\|D_{f\Delta}\pi\right\|-D_{1,2\Delta}\pi\right]$
s_{1c}	I	--	$\left[0,\ 2\pi/3\right]$
	II	--	$\left[0,\ 2\pi/3+\left\|D_{f\Delta}\pi\right\|\right]$
s_{2a}	I	$\left[D_{f,1}\pi,\ D_{f,1}\pi+D_{2,1\Delta}\pi\right]$	$\left(D_{f,1}\pi+D_{2,1\Delta}\pi,\ 2\pi/3+D_{f,2}\pi\right]$
	II	$\left[D_{f,1}\pi,\ D_{f,1}\pi+D_{2,1\Delta}\pi\right]$	$\left(D_{f,1}\pi+D_{2,1\Delta}\pi,\ 2\pi/3+D_{f,1}\pi\right]$
s_{2b}	I	$\left(2\pi/3+D_{f,2}\pi-D_{2,2\Delta}\pi,\ 2\pi/3+D_{f,2}\pi\right]$	$\left[D_{f,1}\pi,\ 2\pi/3+D_{f,2}\pi-D_{2,2\Delta}\pi\right]$
	II	$\left(2\pi/3+D_{f,1}\pi-D_{2,2\Delta}\pi,\ 2\pi/3+D_{f,1}\pi\right]$	$\left[D_{f,1}\pi,\ 2\pi/3+D_{f,1}\pi-D_{2,2\Delta}\pi\right]$
s_{2c}	I	--	$\left[D_{f,1}\pi,\ 2\pi/3+D_{f,2}\pi\right]$
	II	--	$\left[D_{f,1}\pi,\ 2\pi/3+D_{f,1}\pi\right]$

illustrated in Fig. 20) at $\theta = 2\pi/3$ is derived as

$$\vec{i}_{L1}\left(\frac{2\pi}{3}\right)=I_{eq1}\begin{bmatrix}e^{j0^\circ}\cdot\kappa\cdot\left(\Phi\left(D_{1,1\Delta}\right)-1\right)\\ +e^{j120^\circ}\left(1-\Phi\left(-D_{1,2\Delta}\right)\right)\end{bmatrix}+\kappa\cdot\vec{i}_{L1}\left(0\right). \tag{21}$$

On the other side, by referring to (A-14) and (A-15), the steady-state currents in subcircuit I at $\theta = 0$ and $2\pi/3$ are given by

$$\begin{aligned}&\vec{i}_{L1}\left(0\right)\\&=I_{eq1}\frac{e^{j0^\circ}\cdot\boldsymbol{\kappa}\cdot\left(\Phi\left(D_{1,1}\right)-1\right)+e^{j120^\circ}\left(1-\Phi\left(-D_{1,1}\right)\right)}{e^{j120^\circ}-\kappa\cdot e^{j0^\circ}},\\&\vec{i}_{L1}\left(\frac{2\pi}{3}\right)\\&=I_{eq1}\frac{e^{j120^\circ}\cdot\boldsymbol{\kappa}\cdot\left(\Phi\left(D_{1,2}\right)-1\right)+e^{j240^\circ}\left(1-\Phi\left(-D_{1,2}\right)\right)}{e^{j120^\circ}-\kappa\cdot e^{j0^\circ}}.\end{aligned} \tag{22}$$

By substituting (22) into (21), the intermediate duty cycles can be calculated with respect to $D_{1,1}$ and $D_{1,2}$. Additionally, the first-order approximation of the exponential function is used in the derivation, which is expressed as

$$\Phi\left(D\right)=e^{\frac{DT_s}{2\tau}}\approx 1+\frac{DT_s}{2\tau}.$$

Consequently, the expressions of $D_{1,1\Delta}$ and $D_{1,2\Delta}$ are obtained as

$$\begin{aligned}D_{1,1\Delta}&=\frac{\left(\kappa^2+\kappa-1\right)D_{1,1}+2D_{1,2}}{\kappa^2+\kappa+1},\\D_{1,2\Delta}&=\frac{2\kappa^2 D_{1,1}+\left(-\kappa^2+\kappa+1\right)D_{1,2}}{\kappa^2+\kappa+1}.\end{aligned} \tag{23}$$

For the V_2-side bridge, the transient process starts at $\theta = D_{f,1}\pi$ and ends at $\theta = 2\pi/3 + D_{f,2}\pi$. The transient process lasts for $2\pi/3 + D_{f\Delta}\pi$. During the transient process, $D_{2,1\Delta}$ is loaded for s_{2a}, and $D_{2,2\Delta}$ is loaded for s_{2b}. Accordingly, the current vectors of three phases at $\theta = 2\pi/3 + D_{f,2}\pi$ are expressed as

$$\begin{aligned}\vec{i}_{L2a}\left(\frac{2\pi}{3}+D_{f,2}\pi\right)&=I_{eq2}e^{j0^\circ}\cdot\boldsymbol{\kappa}\cdot\Phi\left(-D_{f\Delta}\right)\\&\quad\cdot\left(\Phi\left(D_{2,1\Delta}\right)-1\right)\\&\quad+\boldsymbol{\kappa}\cdot\Phi\left(-D_{f\Delta}\right)\cdot\vec{i}_{L2a}\left(D_{f,1}\pi\right),\\\vec{i}_{L2b}\left(\frac{2\pi}{3}+D_{f,2}\pi\right)&=I_{eq2}e^{j120^\circ}\cdot\left(1-\Phi\left(-D_{2,2\Delta}\right)\right)\\&\quad+\boldsymbol{\kappa}\cdot\Phi\left(-D_{f\Delta}\right)\cdot\vec{i}_{L2b}\left(D_{f,1}\pi\right),\\\vec{i}_{L2c}\left(\frac{2\pi}{3}+D_{f,2}\pi\right)&=\boldsymbol{\kappa}\cdot\Phi\left(-D_{f\Delta}\right)\cdot\vec{i}_{L2c}\left(D_{f,1}\pi\right).\end{aligned} \tag{24}$$

By substituting (24) into (A-6), it can be obtained that

$$\begin{aligned}&\vec{i}_{L2}\left(\frac{2\pi}{3}+D_{f,2}\pi\right)\\&=I_{eq2}\begin{bmatrix}e^{j0^\circ}\cdot\boldsymbol{\kappa}\cdot\Phi\left(-D_{f\Delta}\right)\cdot\left(\Phi\left(D_{2,1\Delta}\right)-1\right)\\+e^{j120^\circ}\cdot\left(1-\Phi\left(-D_{2,2\Delta}\right)\right)\end{bmatrix}\\&\quad+\boldsymbol{\kappa}\cdot\Phi\left(-D_{f\Delta}\right)\cdot\vec{i}_{L2}\left(D_{f,1}\pi\right).\end{aligned} \tag{25}$$

At $\theta = D_{f,1}\pi$, the phase current is in the steady state with $D_2 = D_{2,1}$. After the transient process, the phase current is expected to achieve the steady state with $D_2 = D_{2,2}$ at $\theta = 2\pi/3 + D_{f,2}\pi$. By referring to (A-16), the resulting currents in subcircuit II (as shown in Fig. 20) at $\theta = D_{f,1}\pi$ and $2\pi/3 +$

$D_{f,2}\pi$ are given by

$$\vec{i}_{L2}\left(D_{f,1}\pi\right) = I_{eq2}\frac{e^{j0^\circ}\cdot\boldsymbol{\kappa}\cdot\left(\Phi\left(D_{2,1}\right)-1\right)+e^{j120^\circ}\left(1-\Phi\left(-D_{2,1}\right)\right)}{e^{j120^\circ}-\boldsymbol{\kappa}\cdot e^{j0^\circ}},$$

$$\vec{i}_{L2}\left(\frac{2\pi}{3}+D_{f,2}\pi\right) = I_{eq2}\frac{e^{j120^\circ}\cdot\boldsymbol{\kappa}\cdot\left(\Phi\left(D_{2,2}\right)-1\right)+e^{j240^\circ}\left(1-\Phi\left(-D_{2,2}\right)\right)}{e^{j120^\circ}-\boldsymbol{\kappa}\cdot e^{j0^\circ}}. \quad (26)$$

By substituting (26) into (25), the intermediate duty cycles can be calculated with respect to $D_{2,1}$ and $D_{2,2}$. For simplicity, the first-order approximation is only used for the exponential functions with D_1 and D_2. As a result, the expressions of $D_{2,1\Delta}$ and $D_{2,2\Delta}$ are calculated as

$$D_{2,1\Delta} = \frac{\Phi\left(-D_{f\Delta}\right)\cdot\left(\boldsymbol{\kappa}^2+\boldsymbol{\kappa}-1\right)D_{2,1}+2D_{2,2}}{\Phi\left(-D_{f\Delta}\right)\cdot\left(\boldsymbol{\kappa}^2+\boldsymbol{\kappa}+1\right)},$$

$$D_{2,2\Delta} = \frac{2\boldsymbol{\kappa}^2\cdot\Phi\left(-D_{f\Delta}\right)\cdot D_{2,1}+\left(-\boldsymbol{\kappa}^2+\boldsymbol{\kappa}+1\right)D_{2,2}}{\boldsymbol{\kappa}^2+\boldsymbol{\kappa}+1}. \quad (27)$$

As mentioned before, a low R_s is preferred for reducing the conduction losses. Thus, the time constant τ is large in actual applications. On the other hand, the switching period T_s of the converter is small due to a high switching frequency. On condition that T_s/τ is very small, it can be found that

$$\Phi\left(-D_{f\Delta}\right) = e^{-\frac{D_{f\Delta}T_s}{2\tau}} \approx 1.$$

On this basis, the intermediate duty cycles for the V_2-side bridge are approximated by

$$D_{2,1\Delta} = \frac{\left(\boldsymbol{\kappa}^2+\boldsymbol{\kappa}-1\right)D_{2,1}+2D_{2,2}}{\boldsymbol{\kappa}^2+\boldsymbol{\kappa}+1},$$

$$D_{2,2\Delta} = \frac{2\boldsymbol{\kappa}^2 D_{2,1}+\left(-\boldsymbol{\kappa}^2+\boldsymbol{\kappa}+1\right)D_{2,2}}{\boldsymbol{\kappa}^2+\boldsymbol{\kappa}+1}. \quad (28)$$

By comparing (23) and (28), it is obvious that the expressions of $D_{2,1\Delta}$ and $D_{2,2\Delta}$ have the same forms with those of $D_{1,1\Delta}$ and $D_{1,2\Delta}$. In actual applications, the FTCC block is inserted into the forward path of the closed-loop control system, as shown in Fig. 8. The FTCC block records the input control parameters, which are compared with the control parameters in the last period. In case the control parameters are updated, the FTCC block calculates the intermediate duty cycles, and the driving pulses are generated according to the operating principles of FTCC. The proposed current control method enables the converter to transfer from one steady state to another within about one-third switching period.

V. Experimental Results

Experimental results of a 3p-DAB converter are presented in this section to verify the theoretical analysis. Table II shows the converter specifications. The primary to secondary turns ratio of the transformer is 1:1, and the voltage conversion ratio varies with the voltage of the V_2 port. Thus, the aforementioned analysis is verified with varied voltage conversion ratios. Hall-effect sensors are used in the implementation to measure current waveforms and voltage signals. The entire control is implemented by using a TMS320F28335 DSP from TI.

TABLE II
Experimental Prototype Characteristics

Maximum output power (P_{omax})	1100W
Switching frequency (f_s)	20kHz
V_1-port dc voltage (V_1)	100V
V_2-port dc voltage (V_2)	60V~80V
Transformer turns ratio (N_{12})	1:1
Equivalent series inductance (L_s)	35μH
Equivalent series resistance (R_s)	0.2Ω

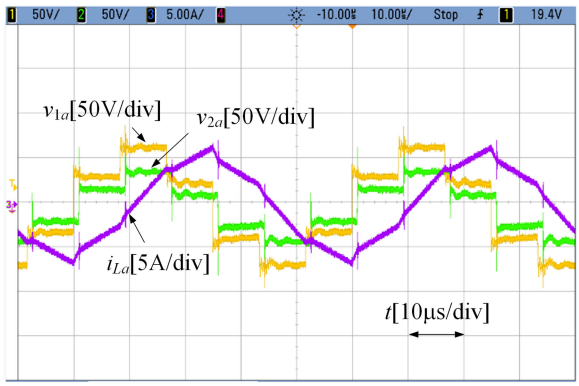

(a)

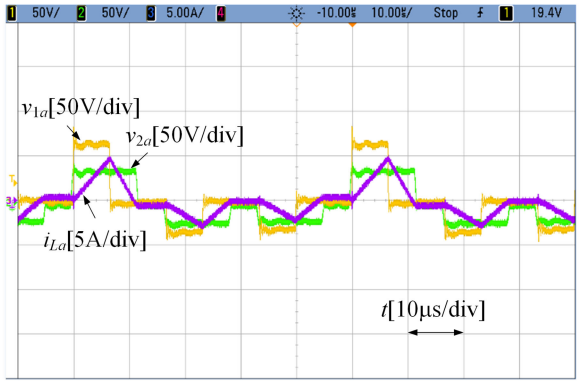

(b)

Fig. 12. Operating waveforms of the 3p-DAB. (a) PS control. (b) Optimized modulation strategy.

Fig. 12 illustrates the operating waveforms of the 3p-DAB where V_2 is maintained at 60 V and the transmission power is 100 W. The voltage conversion ratio is 0.6 here. At this power level, the 3p-DAB is operated under the triangular current mode when the optimized modulation strategy is applied. It is demonstrated that the rms current decreases from 3.97 A with PS control to 1.63 A with the optimized modulation strategy. Details of turn-ON transitions of T_{21} and T_{24} are depicted in Fig. 13, where v_{ds} and v_{gs} denote the drain–source and gate–source voltages of the active switch. The operating conditions are the same as those in Fig. 12. It is evident that both T_{21} and T_{24} suffer HS with PS control. When the optimized modulation strategy is applied, T_{21}

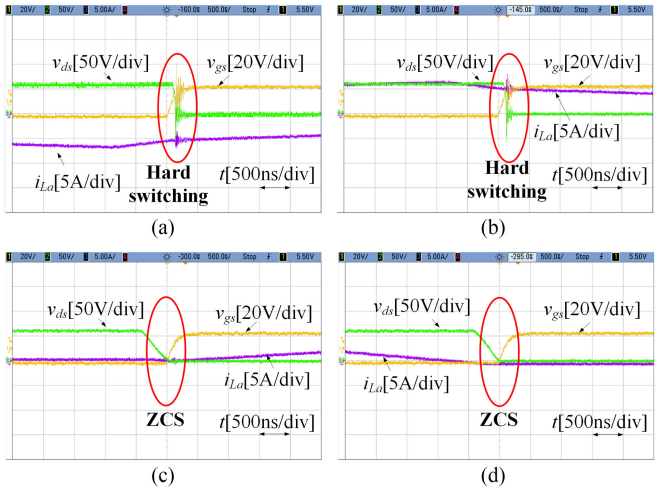

Fig. 13. Turn-ON transitions of T_{21} and T_{24}. (a) T_{21} with PS control. (b) T_{24} with PS control. (c) T_{21} with the optimized modulation strategy. (d) T_{24} with the optimized modulation strategy.

and T_{24} are switched at ZCS. The proposed modulation strategy extends the soft-switching operating range compared with PS control. Actually, full soft-switching operation is achieved for the 3p-DAB at low loads by using the optimized modulation strategy. Since the conduction losses as well as the switching losses decrease, the efficiency increases from 90.75% with PS control to 96.76% with the optimized modulation strategy. The efficiency of the 3p-DAB is boosted significantly at low loads.

Fig. 14 compares the measured rms currents and efficiencies of the converter with PS control and the proposed optimized modulation strategy, where bidirectional power-transfer operations are investigated. A negative P_o indicates that the power transfers from V_2 port to V_1 port. The values of V_2 are 60 and 80 V. Thus, the corresponding voltage conversion ratios are 0.6 and 0.8. It can be concluded that the optimized modulation strategy has a lower rms current in most of the load range. At high loads, the optimized modulation evolves into PS control. The efficiency is also improved with the optimized modulation strategy especially when the converter is operated at low loads with a voltage conversion ratio far away from unity. The experimental results coincide with the theoretical analysis.

The performance of the closed-loop control strategy is verified by the steady state and dynamic response tests. V_1 is defined as the input and maintained at 100 V. V_2 is the output, which is regulated by the controller. In practice, the desired optimal duty cycles are calculated off-line and prestored in the memory of the microcontroller. Then, the optimal duty cycles with respect to the required transmission power and the voltage conversion ratio are obtained on-line by using the method of a lookup table. The slow loop block is designed as an integration link with a large time constant and its bandwidth is 1/10 of the voltage loop's bandwidth. Fig. 15 shows the steady-state waveforms of the phase currents and the output voltage, where four steady-state operating points with different values of the output voltage and the transmission power are investigated, i.e., (60 V, 400 W), (60 V, 600 W), (80 V, 400 W), and (80 V, 800 W). The measured output voltages are 59.97, 60.10, 79.80, and 79.70 V, while the

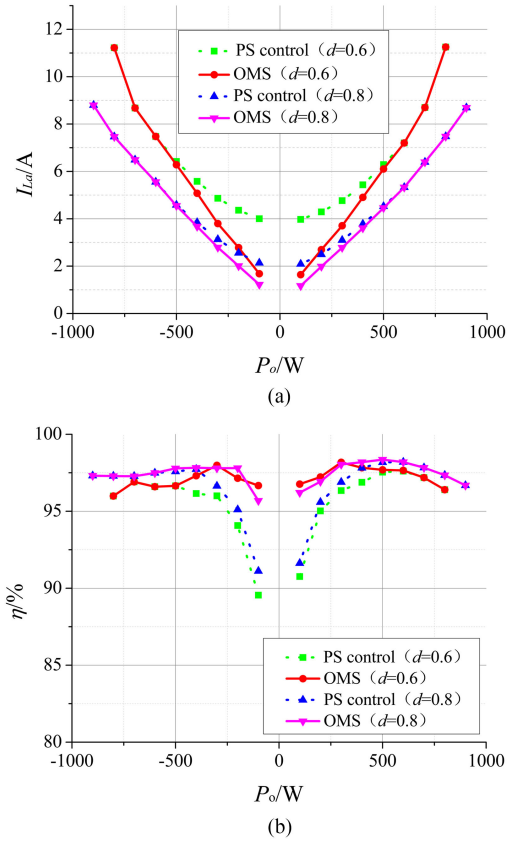

Fig. 14. Comparison of rms phase currents and efficiencies with PS control and the optimized modulation strategy (OMS). (a) RMS phase current. (b) Efficiency.

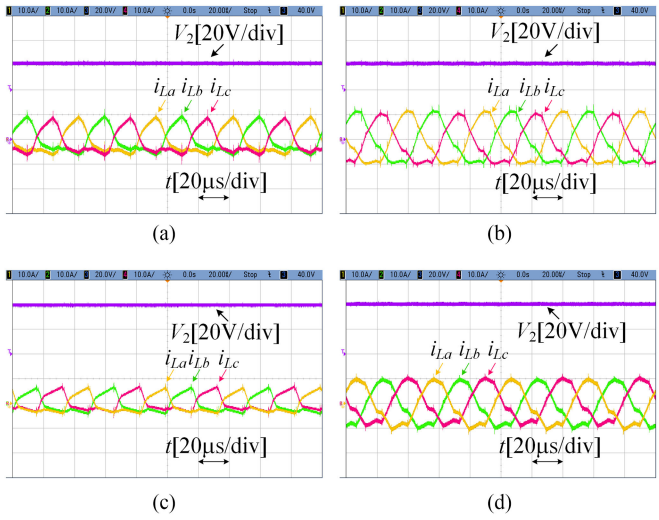

Fig. 15. Steady-state waveforms of the phase currents and the output voltage with the closed-loop control strategy. (a) $V_2 = 60$ V, $P_o = 400$ W. (b) $V_2 = 60$ V, $P_o = 600$ W. (c) $V_2 = 80$ V, $P_o = 400$ W. (d) $V_2 = 80$ V, $P_o = 800$ W.

relative errors are 0.05%, 0.17%, 0.25%, and 0.37%, respectively. It is evident that the closed-loop control strategy ensures the converter to output the required voltage accurately. Table III lists the optimal duty cycles determined by the controller and that from the theoretical calculation. The actual optimal control

TABLE III
CALCULATED AND MEASURED OPTIMAL DUTY CYCLES

Output voltage	Transmission power	Duty cycle D_1			Duty cycle D_2		
		Calculated value	Measured value	Relative error	Calculated value	Measured value	Relative error
60V	400W	0.2598	0.2550	1.85%	0.3885	0.3849	0.93%
60V	600W	0.4159	0.4213	1.30%	0.4643	0.4632	0.24%
80V	400W	0.3152	0.3093	1.87%	0.3786	0.3740	1.21%
80V	800W	0.4545	0.4493	1.14%	0.4673	0.4641	0.68%

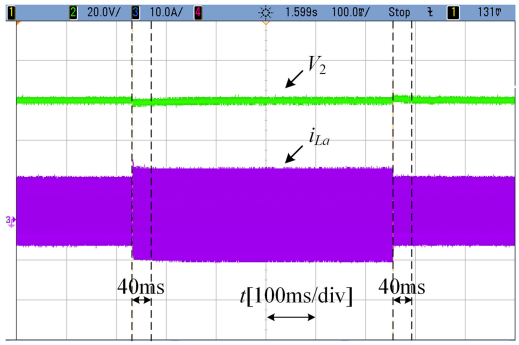

Fig. 16. Dynamic response when the 3p-DAB is operated under DCC.

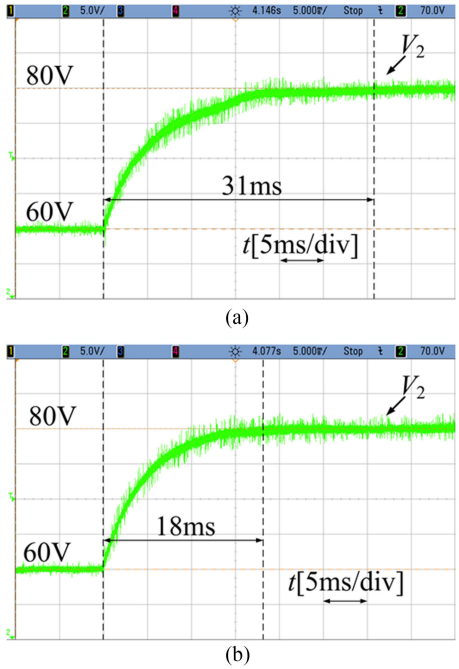

Fig. 17. Dynamic responses of the converter with the constant limit and the proposed optimized limiting link. (a) Constant limit 0.5. (b) Optimized limiting link.

parameters agree with the theoretical values basically. The optimized modulation strategy is well implemented in the practical operation. The minor errors are caused by the dead time, the power losses, and the errors during the look-up process.

The dynamic behavior of the 3p-DAB with the closed-loop control strategy is tested by applying load steps from 400 to 600 W and back to 400 W. V_1 is maintained at 100 V, and V_2 is regulated at 60 V. The resulting waveforms are shown in Fig. 16. It can be concluded that the dynamic response of the converter is stable and well damped with the designed closed-loop control strategy. Fig. 17(a) presents the dynamic response of the converter with a constant limit 0.5, while Fig. 17(b) shows the dynamic response of the converter with the proposed optimized limiting link. The load resistor is 10 Ω, and the voltage reference steps from 60 to 80 V. The measured settling times are 31 and 18 ms. It can be concluded that the proposed optimized limiting link improves the dynamic behavior of the converter under DCC.

The proposed FTCC method is validated by both the open-loop and the closed-loop tests. V_1 is the input and maintained at 100 V. V_2 is the output, which is regulated to be 60 V. The transmission power steps between 400 and 600 W. Fig. 18 presents the phase currents of the converter under the open-loop control. The conventional method and the FTCC method are investigated. As depicted in Fig. 18(a) and (b), when the conventional method is applied, it takes the phase currents about 380 μs to achieve the target steady states in the cases of increasing power and decreasing power. Moreover, significant dc bias and unbalance can be observed in the phase currents, where the peak current is up to 13.2 A. Fig. 18(c) and (d) illustrates the transitions of the phase currents in the cases of increasing power and decreasing power when the FTCC method is applied. It takes the phase currents about 22 μs to achieve the target steady states. There are also no dc bias and unbalance in the phase currents during the transient interval.

Fig. 19 presents the phase currents of the converter with the closed-loop control strategy. As depicted in Fig. 19(a) and (b), when the conventional method is applied, the settling time of the transient interval is about 1.3 ms. Significant dc bias and unbalance can be also observed in the phase currents. When the FTCC method is applied, the FTCC block is inserted into the forward path of the closed-loop control system, and the intermediate duty cycles are calculated. The resulting current waveforms are shown in Fig. 19(c) and (d). It is evident that the FTCC method balances the phase currents rapidly, thereby avoiding oscillations in currents.

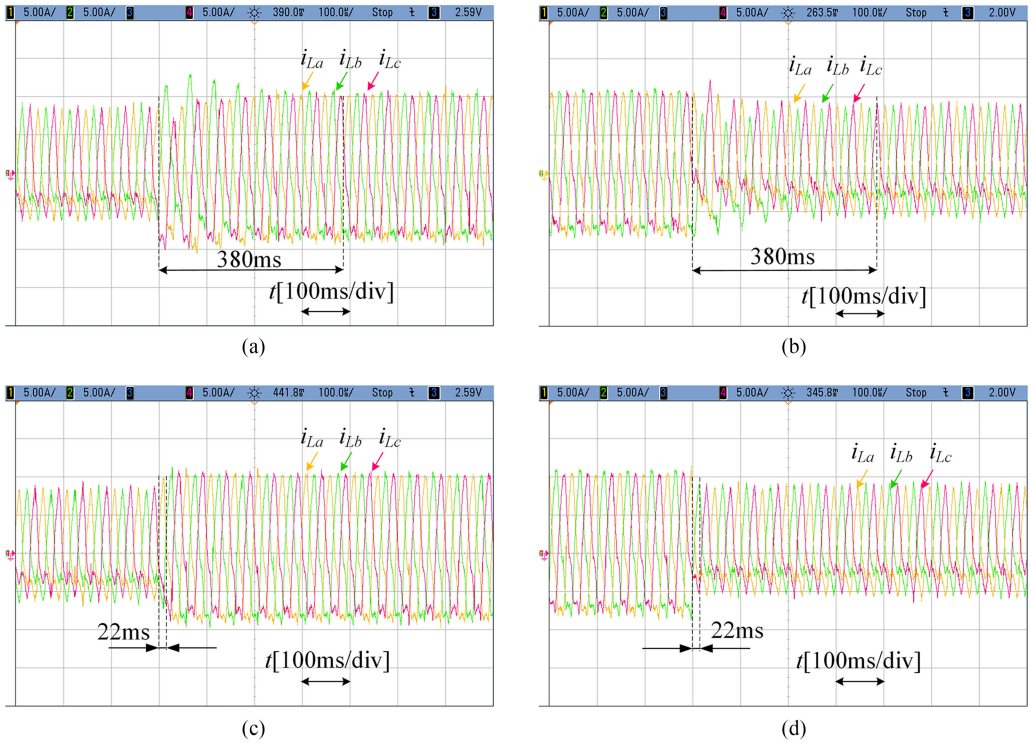

Fig. 18. Phase currents of the converter under the open-loop control. (a) Conventional method when increasing power. (b) Conventional method when decreasing power. (c) FTCC when increasing power. (d) FTCC when decreasing power.

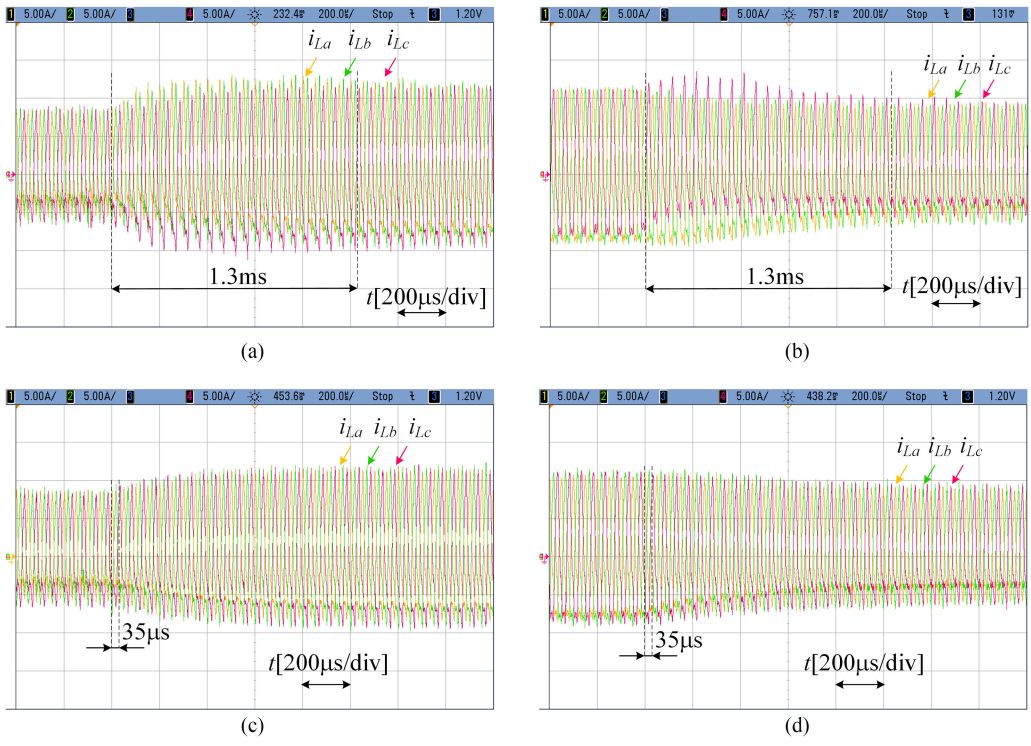

Fig. 19. Phase currents of the converter under the closed-loop control. (a) Conventional method when increasing power. (b) Conventional method when decreasing power. (c) FTCC when increasing power. (d) FTCC when decreasing power.

VI. Conclusion

Based on DCC, this paper proposes an optimized modulation strategy to minimize the conduction losses of the 3p-DAB in the whole load range. Simultaneously, the proposed modulation strategy extends the soft-switching range of the converter. High efficiency is achieved for the converter consequently. This paper develops a novel algorithm based on the interior point method to derive the global minimum rms current and the optimal control parameters. This algorithm has great universality and can be extended to other optimization problems of the 3p-DAB. This paper also presents detailed descriptions on the closed-loop control of the 3p-DAB under DCC. An optimized limiting link is introduced into the closed-loop control blocks, which improves the dynamic response of the converter with variable duty cycles. Moreover, the FTCC method is proposed to improve the transient performance. The analytical expressions of the intermediate duty cycles are derived. On this basis, the FTCC block is inserted into the forward path of the closed-loop control system, which enables the converter to transfer from one steady state to another within about one-third switching period theoretically. Therefore, the proposed control method balances the transformer currents rapidly and avoids possible oscillations in dc currents. This paper presents a systematic analysis of the optimized modulation and dynamic control of the 3p-DAB under DCC. Accordingly, a unified implement standard is developed for the 3p-DAB under DCC in this paper.

Appendix

The three-phase quantities (u_a, u_b, u_c) can be transformed into one time-dependent space vector $\vec{u}$ by the amplitude invariant 3-to-2 phase transformation that is expressed as

$$\vec{u} = \vec{u}_a + \vec{u}_b + \vec{u}_c = \frac{2}{3}\left(u_a + e^{j120^\circ}u_b + e^{j240^\circ}u_c\right). \quad \text{(A-1)}$$

The voltages and currents in the transformer of the 3p-DAB are transformed into $\alpha\beta$ coordinates, and the corresponding space vectors $\vec{v}_1$, $\vec{v}_2$, and $\vec{i}_L$ are given by

$$\begin{aligned}\vec{v}_1 &= \vec{v}_{1a} + \vec{v}_{1b} + \vec{v}_{1c}\\ \vec{v}_2 &= \vec{v}_{2a} + \vec{v}_{2b} + \vec{v}_{2c}\\ \vec{i}_L &= \vec{i}_{La} + \vec{i}_{Lb} + \vec{i}_{Lc}\end{aligned} \quad \text{(A-2)}$$

where $\vec{v}_{1a}$, $\vec{v}_{1b}$, and $\vec{v}_{1c}$ are the space vectors of phase voltages on the V_1 side, $\vec{v}_{2a}$, $\vec{v}_{2b}$, and $\vec{v}_{2c}$ are the space vectors of phase voltages on the V_2 side, $\vec{i}_{La}$, $\vec{i}_{Lb}$, and $\vec{i}_{Lc}$ are the space vectors of phase currents on the V_1 side, and $\vec{v}_{1a}$, $\vec{v}_{1b}$, $\vec{v}_{1c}$, $\vec{v}_{2a}$, $\vec{v}_{2b}$, and $\vec{v}_{2c}$ are expressed as

$$\begin{aligned}\vec{v}_{1a}(t) &= \frac{2}{3}V_1 s_{1a}(t)\, e^{j0^\circ}, \vec{v}_{1b}(t) = \frac{2}{3}V_1 s_{1b}(t)\, e^{j120^\circ}\\ \vec{v}_{1c}(t) &= \frac{2}{3}V_1 s_{1c}(t)\, e^{j240^\circ}, \vec{v}_{2a}(t) = \frac{2}{3}V_2 s_{2a}(t)\, e^{j0^\circ}\\ \vec{v}_{2b}(t) &= \frac{2}{3}V_2 s_{2b}(t)\, e^{j120^\circ}, \vec{v}_{2c}(t) = \frac{2}{3}V_2 s_{2c}(t)\, e^{j240^\circ}.\end{aligned} \quad \text{(A-3)}$$

By neglecting the magnetizing inductances, the equivalent circuit of the 3p-DAB in $\alpha\beta$ coordinates is illustrated in Fig. 20. In order to simplify the analysis, the values of R_a, R_b, and R_c are all equal to R_s herein. It can be concluded that the equivalent circuit is a first-order circuit, and the differential equation is derived as

$$\frac{d\vec{i}_L}{dt} = \frac{1}{L_s}\left(\vec{v}_1 - R_s\vec{i}_L - N_{12}\vec{v}_2\right). \quad \text{(A-4)}$$

By solving the first-order differential equation, the current response is described as

$$\vec{i}_L(t) = \vec{i}_L(\infty) + \left[\vec{i}_L(0) - \vec{i}_L(\infty)\right]e^{-\frac{t}{\tau}} \quad \text{(A-5)}$$

where $\vec{i}_L(\infty) = (\vec{v}_1 - N_{12}\vec{v}_2)/R_s$, $\vec{i}_L(0)$ is the initial current at $t = 0$, and $\tau = L_s/R_s$ is the time constant.

The equivalent circuit is a linear circuit that consists of two linear elements and two independent sources. According to the superposition theorem, the equivalent circuit can be divided into two subcircuits (i.e., subcircuits I and II), as shown in Fig. 20. Each subcircuit has only one independent source (one voltage vector). The current vectors satisfy that $\vec{i}_L = \vec{i}_{L1} - \vec{i}_{L2}$, where $\vec{i}_{L1}$ denotes the current in subcircuit I, and $\vec{i}_{L2}$ denotes the current in subcircuit II. There are three control parameters when the 3p-DAB is operated under DCC. It can be found that D_1 only influences the voltage vector $\vec{v}_1$, while D_2 only influences the voltage vector $\vec{v}_2$. As for D_f, if the switching time for one bridge is defined as zero time, D_f only influences the voltage vector of the other bridge. It can be concluded that the control parameters are decoupled for the voltage vectors. Additionally, each subcircuit can be further divided into three secondary subcircuits on the basis of the superposition theorem and (A-2), as illustrated in Fig. 20. $\vec{i}_{L1}$ and $\vec{i}_{L2}$ are divided into $\vec{i}_{L1a}$, $\vec{i}_{L1b}$, $\vec{i}_{L1c}$, $\vec{i}_{L2a}$, $\vec{i}_{L2b}$, and $\vec{i}_{L2c}$ accordingly. It is obvious that

$$\begin{aligned}\vec{i}_{L1} &= \vec{i}_{L1a} + \vec{i}_{L1b} + \vec{i}_{L1c},\\ \vec{i}_{L2} &= \vec{i}_{L2a} + \vec{i}_{L2b} + \vec{i}_{L2c}.\end{aligned} \quad \text{(A-6)}$$

From Fig. 20, the following first-order differential equations are derived as

$$\begin{aligned}\frac{d\vec{i}_{L1x}}{dt} &= \frac{1}{L_s}\left(\vec{v}_{1x} - R_s\vec{i}_{L1x}\right)\\ \frac{d\vec{i}_{L2x}}{dt} &= \frac{1}{L_s}\left(N_{12}\vec{v}_{2x} - R_s\vec{i}_{L2x}\right)\end{aligned} \quad \text{(A-7)}$$

where the subscript *x* denotes *a*, *b*, or *c*. The secondary subcircuits are independent of each other as well and can be analyzed respectively. Then, by combining the operations of subcircuits according to (A-2), the performance of the whole three-phase circuit can be investigated.

Steady-state phase currents can be calculated. Without loss of generality, subcircuit I is discussed, and the center of the driving pulse for T_{11} is defined as zero time in the following. Fig. 21 illustrates the switching functions used in subcircuit I, where the calibration of the transverse-axis is given by the radian.

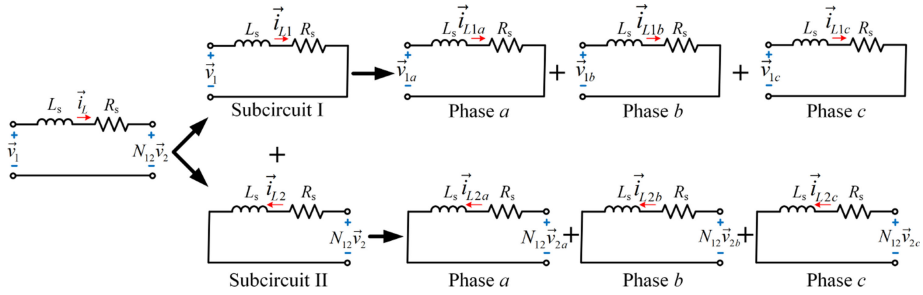

Fig. 20. Equivalent circuits of a 3p-DAB converter in $\alpha\beta$ coordinates.

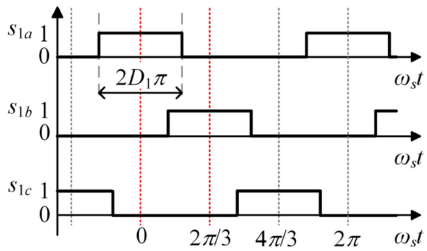

Fig. 21. Waveforms of the switching functions used in subcircuit I.

In the first one-third period, the value of s_{1a} is 1 in $[\,0, D_1\pi]$, and 0 in $(D_1\pi, 2\pi/3]$. With (A-5) and (A-7), the resulting currents of phase a at $\theta = D_1\pi$ and $2\pi/3$ can be obtained as

$$\vec{i}_{L1a}\left(D_1\pi\right) = I_{eq1}e^{j0^\circ} + \left(\vec{i}_{L1a}\left(0\right) - I_{eq1}e^{j0^\circ}\right)\cdot\Phi\left(D\right)\big|_{D=-D_1} \tag{A-8}$$

$$\vec{i}_{L1a}\left(\frac{2\pi}{3}\right) = \boldsymbol{\kappa}\cdot\vec{i}_{L1a}\left(D_1\pi\right)\cdot\Phi\left(D\right)\big|_{D=D_1} \tag{A-9}$$

where $I_{eq1} = 2V_1/(3R_s)$, $\Phi(D) = e^{DT_s/(2\tau)}$, and $\kappa = e^{-T_s/(3\tau)}$. By substituting (A-8) into (A-9), the expression of $\vec{i}_{L1a}(2\pi/3)$ with respect to $\vec{i}_{L1a}(0)$ is derived as

$$\vec{i}_{L1a}\left(\frac{2\pi}{3}\right) = I_{eq1}e^{j0^\circ}\cdot\kappa\cdot\left(\Phi\left(D_1\right)-1\right) + \kappa\cdot\vec{i}_{L1a}\left(0\right). \tag{A-10}$$

In addition, the value of s_{1b} is 0 in $[\,0{,}2\pi/3 - D_1\pi]$, and 1 in $(2\pi/3 - D_1\pi{,}2\pi/3]$, while the value of s_{1c} is 0 in the first one-third period. After the same derivation, the resulting currents of phases b and c at $\theta = 2\pi/3$ are obtained as

$$\vec{i}_{L1b}\left(\frac{2\pi}{3}\right) = I_{eq1}e^{j120^\circ}\cdot\left(1-\Phi\left(-D_1\right)\right) + \boldsymbol{\kappa}\cdot\vec{i}_{L1b}\left(0\right), \tag{A-11}$$

$$\vec{i}_{L1c}\left(\frac{2\pi}{3}\right) = \boldsymbol{\kappa}\cdot\vec{i}_{L1c}\left(0\right). \tag{A-12}$$

By substituting (A-10)–(A-12) into (A-6), the current vector in subcircuit I at $\theta = 2\pi/3$ is expressed as

$$\vec{i}_{L1}\left(\frac{2\pi}{3}\right) = I_{eq1}\left[e^{j0^\circ}\cdot\boldsymbol{\kappa}\cdot\left(\Phi\left(D_1\right)-1\right) + e^{j120^\circ}\left(1-\Phi\left(-D_1\right)\right)\right] + \boldsymbol{\kappa}\cdot\vec{i}_{L1}\left(0\right). \tag{A-13}$$

Due to the symmetry of three phases, $\vec{i}_{L1}(2\pi/3)$ and $\vec{i}_{L1}(0)$ are shifted by 120° in the steady state. Thus, the current vector has the feature that

$$\vec{i}_{L1}\left(2\pi/3\right) = \vec{i}_{L1}\left(0\right)e^{j120^\circ}. \tag{A-14}$$

With (A-13) and (A-14), the starting current in subcircuit I is calculated as

$$\vec{i}_{L1}\left(0\right) = I_{eq1}\frac{e^{j0^\circ}\cdot\boldsymbol{\kappa}\cdot\left(\Phi\left(D_1\right)-1\right) + e^{j120^\circ}\left(1-\Phi\left(-D_1\right)\right)}{e^{j120^\circ} - \boldsymbol{\kappa}\cdot e^{j0^\circ}}. \tag{A-15}$$

By applying a similar derivation, the starting current in subcircuit II can be calculated, which is given by

$$\vec{i}_{L2}\left(0\right) = I_{eq2}\frac{e^{j0^\circ}\cdot\boldsymbol{\kappa}\cdot\left(\Phi\left(D_2\right)-1\right) + e^{j120^\circ}\left(1-\Phi\left(-D_2\right)\right)}{e^{j120^\circ} - \boldsymbol{\kappa}\cdot e^{j0^\circ}} \tag{A-16}$$

where $I_{eq2} = 2N_{12}V_2/(3R_s)$.

REFERENCES

[1] B. Zhao, Q. Song, W. H. Liu, and Y. D. Sun, "Overview of dual-active-bridge isolated bidirectional dc–dc converter for high-frequency-link power-conversion system," *IEEE Trans. Power Electron.*, vol. 29, no. 8, pp. 4091–4106, Aug. 2014.

[2] H. Fan and H. Li, "High-frequency transformer isolated bidirectional dc–dc converter modules with high efficiency over wide load range for 20 kVA solid-state transformer," *IEEE Trans. Power Electron.*, vol. 26, no. 12, pp. 3599–3608, Dec. 2011.

[3] N. M. L. Tan, T. Abe, and H. Akagi, "Design and performance of a bidirectional isolated dc-dc converter for a battery energy storage system," *IEEE Trans. Power Electron.*, vol. 27, no. 3, pp. 1237–1248, Mar. 2012.

[4] S. P. Engel, M. Stieneker, N. Soltau, S. Rabiee, H. Stagge, and R. W. De Doncker, "Comparison of the modular multilevel dc converter and the dual-active bridge converter for power conversion in HVDC and MVDC grids," *IEEE Trans. Power Electron.*, vol. 30, no. 1, pp. 124–137, Jan. 2015.

[5] S. S. Williamson, A. K. Rathore, and F. Musavi, "Industrial electronics for electric transportation: Current state-of-the-art and future challenges," *IEEE Trans. Ind. Electron.*, vol. 62, no. 5, pp. 3021–3032, May 2015.

[6] R. W. De Doncker, D. M. Divan, and M. H. Kheraluwala, "A three phase soft-switched high-power-density dc/dc converter for high-power applications," *IEEE Trans. Ind. Appl.*, vol. 27, no. 1, pp. 63–73, Jan./Feb. 1991.

[7] R. O. Nunez, G. G. Oggier, F. Botteron, and G. O. Garcia, "Analysis of the transformer influence on a three-phase dual active bridge dc-dc converter," *IEEE Latin Amer. Trans.*, vol. 14, no. 7, pp. 3048–3055, Jul. 2016.

[8] N. H. Baars, J. Everts, C. G. E. Wijnands, and E. A. Lomonova, "Performance evaluation of a three-phase dual active bridge dc–dc converter with different transformer winding configurations," *IEEE Trans. Power Electron.*, vol. 31, no. 10, pp. 6814–6823, Oct. 2016.

[9] J. M. Zhang, Z. H. Wang, and S. Shao, "A three-phase modular multilevel dc–dc converter for power electronic transformer applications," *IEEE J. Emerging Sel. Topics Power Electron.*, vol. 5, no. 1, pp. 140–150, Mar. 2017.

[10] D. Segaran, D. G. Holmes, and B. P. Mcgrath, "Comparative analysis of single and three-phase dual active bridge bidirectional dc-dc converters," in *Proc. Australas. Univ. Power Eng. Conf.*, Dec. 2008, pp. 1–6.

[11] H. V. Hoek, M. Neubert, A. Kroeber, and R. W. D. Doncker, "Comparison of a single-phase and a three-phase dual active bridge with low-voltage, high-current output," in *Proc. Int. Conf. Renew. Energy Res. Appl.*, Nov. 2012, pp. 1–6.

[12] N. H. Baars, J. Everts, H. Huisman, J. L. Duarte, and E. A. Lomonova, "A 80-kW isolated dc–dc converter for railway applications," *IEEE Trans. Power Electron.*, vol. 30, no. 12, pp. 6639–6647, Dec. 2015.

[13] J. Riedel, D. G. Holmes, B. P. McGrath, and C. Teixeira, "ZVS soft switching boundaries for dual active bridge dc–dc converters using frequency domain analysis," *IEEE Trans. Power Electron.*, vol. 32, no. 4, pp. 3166–3179, Apr. 2017.

[14] G. G. Oggier, G. O. García, and A. R. Oliva, "Switching control strategy to minimize dual active bridge converter losses," *IEEE Trans. Power Electron.*, vol. 24, no. 7, pp. 1826–1838, Jul. 2009.

[15] G. G. Oggier, G. O. García, and A. R. Oliva, "Modulation strategy to operate the dual active bridge dc–dc converter under soft switching in the whole operating range," *IEEE Trans. Power Electron.*, vol. 26, no. 4, pp. 1228–1236, Apr. 2011.

[16] A. K. Jain and R. Ayyanar, "PWM control of dual active bridge: comprehensive analysis and experimental verification," *IEEE Trans. Power Electron.*, vol. 26, no. 4, pp. 1215–1227, Apr. 2011.

[17] F. Krismer and J. W. Kolar, "Closed form solution for minimum conduction loss modulation of DAB converters," *IEEE Trans. Power Electron.*, vol. 27, no. 1, pp. 174–188, Jan. 2012.

[18] H. Q. Wen, W. D. Xiao, and B. Su, "Nonactive power loss minimization in a bidirectional isolated dc–dc converter for distributed power systems," *IEEE Trans. Ind. Electron.*, vol. 61, no. 12, pp. 6822–6831, Dec. 2014.

[19] H. Hoek, M. Neubert, and R. W. D. Doncker, "Enhanced modulation strategy for a three-phase dual active bridge-boosting efficiency of an electric vehicle converter," *IEEE Trans. Power Electron.*, vol. 28, no. 12, pp. 5499–5507, Dec. 2013.

[20] G. J. Su and L. X. Tang, "A three-phase bidirectional dc-dc converter for automotive applications," in *Proc. IEEE Ind. Appl. Soc. Annu. Meeting*, Oct. 2008, pp. 1–7.

[21] Z. Wang and H. Li, "A soft switching three-phase current-fed bidirectional dc-dc converter with high efficiency over a wide input voltage range," *IEEE Trans. Power Electron.*, vol. 27, no. 2, pp. 669–684, Feb. 2012.

[22] J. Huang, Y. Wang, Z. Q. Li, Y. B. Jiang, and W. J. Lei, "Simultaneous PWM control to operate the three-phase dual active bridge converter under soft switching in the whole load range," in *Proc. IEEE 30th Annu. Appl. Power Electron. Conf. Expo.*, Mar. 2015, pp. 2885–2891.

[23] J. X. Hu, N. Soltau, and R. W. D. Doncker, "Asymmetrical duty-cycle control of three-phase dual-active bridge converter for soft-switching range extension," in *Proc. IEEE Energy Convers. Congr. Expo.*, Sep. 2016, pp. 1–8.

[24] X. D. Li and Y. F. Li, "An optimized phase-shift modulation for fast transient response in a dual-active-bridge converter," *IEEE Trans. Power Electron.*, vol. 29, no. 6, pp. 2661–2665, Jun. 2014.

[25] B. Zhao, Q. Song, W. H. Liu, and Y. M. Zhao, "Transient DC bias and current impact effects of high-frequency-isolated bidirectional dc–dc converter in practice," *IEEE Trans. Power Electron.*, vol. 31, no. 4, pp. 3203–3216, Apr. 2016.

[26] S. Dutta, S. Hazra, and S. Bhattacharya, "A digital predictive current-mode controller for a single-phase high-frequency transformer-isolated dual-active bridge dc-to-dc converter," *IEEE Trans. Ind. Electron.*, vol. 63, no. 9, pp. 5943–5952, Sep. 2016.

[27] S. P. Engel, N. Soltau, H. Stagge, and R. W. D. Doncker, "Dynamic and balanced control of three-phase high-power dual-active bridge dc-dc converters in dc-grid applications," *IEEE Trans. Power Electron.*, vol. 28, no. 4, pp. 1880–1889, Apr. 2013.

[28] S. P. Engel, N. Soltau, H. Stagge, and R. W. D. Doncker, "Improved instantaneous current control for high-power three-phase dual-active bridge dc–dc converters, " *IEEE Trans. Power Electron.*, vol. 29, no. 8, pp. 4067–4077, Aug. 2014.

[29] S. Boyd and L. Vandenberghe, *Convex Optimization*. Cambridge, U.K.: Cambridge Univ. Press, 2009.

[30] R. A. Waltz, J. L. Morales, J. Nocedal, and D. Orban, "An interior algorithm for nonlinear optimization that combines line search and trust region steps," *Math. Program.*, vol. 107, no. 3, pp. 391–408, 2006.

Jun Huang received the B.S. and Ph.D. degrees in electrical engineering from Xi'an Jiaotong University, Xi'an, China, in 2009 and 2016, respectively.

Since 2016, he has been an Engineer with Nari Group Corporation (State Grid Electric Power Research Institute), Nanjing, China. His research interests include high-frequency-link power conversion systems, isolated bidirectional dc–dc converters, high-power insulated-gate bipolar transistor drivers, and electric vehicle drive technologies.

Dr. Huang serves as a Reviewer for various IEEE transactions and other international journals on electrical and electronic engineering.

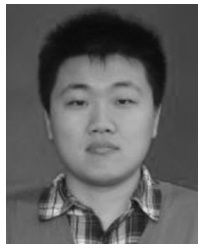

Zhuoqiang Li received the B.S. and M.S. degrees in electrical engineering from Xi'an Jiaotong University, Xi'an, China, in 2014 and 2017, respectively.

Since 2017, he has been an Engineer with United Automotive Electronic Systems Co. Ltd., Shanghai, China. His research interests include bidirectional dc–dc converters.

Ling Shi received the B.S. degree from Xidian University, Xi'an, China, in 2014, and the M.S. degree from Xi'an Jiaotong University, Xi'an, China, in 2017, both in electrical engineering.

Since 2017, she has been an Engineer with Delta Electronics (Shanghai) Co. Ltd., Shanghai, China. Her research interests include modeling and control of dc–dc converters.

Yue Wang (M'05) received the B.S. degree from Xi'an Jiaotong University, Xi'an, China, in 1994, the M.S. degree from Beijing Jiaotong University, Beijing, China, in 2000, and the Ph.D. degree from Xi'an Jiaotong University, in 2004, all in electrical engineering.

He is currently a Full Professor with the School of Electrical Engineering, Xi'an Jiaotong University. His research interests include active power filters, wind power generation, motor drives, multilevel converters, and HVDC.

Jinda Zhu received the B.S. and M.S. degrees in measuring and testing technologies and instruments from the Harbin Institute of Technology, Harbin, China, in 1986 and 1989, respectively.

Since 1989, he has been an Engineer with Nari Group Corporation (State Grid Electric Power Research Institute), Nanjing, China, where he is currently the Vice Chief Engineer. His research interests include the automation of electric power systems, electric power metering systems, and electric vehicle charging technologies